Floodwater Impact on Galveston Bay Phytoplankton Taxonomy, Pigment Composition and Photo-Physiological State following Hurricane Harvey from Field and Ocean Color (Sentinel-3A OLCI) Observations

Bingqing Liu[1], Eurico D'Sa[1*] and Ishan Joshi[1]

[1]Department of Oceanography and Coastal Sciences, Louisiana State University, Baton Rouge, LA 70803, USA
* Corresponding author: ejdsa@lsu.edu

Abstract

Phytoplankton taxonomy, pigment composition and photo-physiological state were studied in Galveston Bay (GB), Texas (USA) following the extreme flooding associated with Hurricane Harvey (August 25–29, 2017) using field and satellite ocean color observations. Percentage of chlorophyll a (Chl a) in different phytoplankton groups were determined from a semi-analytical IOP (inherent optical property) inversion algorithm. The IOP inversion algorithm revealed the dominance of freshwater species (diatom, cyanobacteria and green algae) in the bay following the hurricane passage (September 29, 2017) under low salinity conditions associated with the discharge of floodwaters into GB; 2 months after the hurricane (October 29–30, 2017), under more seasonal salinity conditions, the phytoplankton community transitioned to an increase in small sized groups such as haptophyte and prochlorophyte. Sentinel-3A OLCI-derived Chl a obtained using a red/NIR band ratio algorithm for the turbid estuarine waters was highly correlated ($R^2 > 0.90$) to HPLC-derived Chl a concentrations. Long-term observations of OLCI-derived Chl a (August, 2016-December, 2017) in GB revealed that hurricane-induced Chl a declined to background mean state in late October, 2017. A Non-Negative Least Square (NNLS) inversion model was then applied to OLCI-derived Chl a maps of GB to investigate spatiotemporal variations of phytoplankton diagnostic pigments pre- and post-hurricane; results appeared consistent with extracted phytoplankton taxonomic composition derived from the IOP inversion algorithm and microplankton pictures obtained from an Imaging FlowCytobot (IFCB). OLCI-derived diagnostic pigment distributions also exhibited good agreement with HPLC measurements during both surveys, with mean R^2 ranging from 0.39 for violaxanthin to 0.98 for Chl a. Environmental factors (e.g., floodwaters) combined with phytoplankton taxonomy also strongly modulated phytoplankton physiology in the bay as indicated by measurements of photosynthetic parameters with a Fluorescence Induction and Relaxation (FIRe) system. Phytoplankton in well-mixed waters (mid-bay area) exhibited maximum PSII photochemical efficiency (F_V/F_M) and low effective absorption cross section (σ_{PSII}), while the areas adjacent to the shelf (likely nutrient-limited) showed low F_V/F_M and elevated σ_{PSII} values. Overall, the approach using field and ocean color data combined with inversion models allowed, for the first time, an assessment of phytoplankton response to a large hurricane-related floodwater perturbation in a turbid estuarine environment based on its taxonomy, pigment composition and physiological state.

Key words: Galveston Bay, phytoplankton taxonomy, pigment composition, physiology, ocean color, chlorophyll a, Sentinel-3A OLCI

1. Introduction

Phytoplankton, which form the basis of the aquatic food web, are crucial to marine ecosystems and play a strong role in marine biogeochemical cycling and climate change. Phytoplankton contributes approximately half of the total primary production on Earth, fixing ~50 GT of carbon into organic matter per year through photosynthesis; however, various phytoplankton taxa affect differently the carbon fixation and export (Sathyendranath et al., 2014). Chlorophyll a (Chl a), an essential phytoplankton photosynthetic pigment, has been considered a reliable indicator of phytoplankton biomass and primary productivity in aquatic systems (Bracher et al., 2015). Phytoplankton also contain several accessory pigments such as chlorophyll-b (Chl b), chlorophyll-c (Chl c), photosynthetic carotenoids (PSC) and photo-protective carotenoids (PPC) that are either involved in light harvesting, or in protecting Chl a and other sensitive pigments from photo-damage (Fishwick et al., 2006). Some of PSCs and PPCs are taxa-specific and have been considered as bio-marker pigments: e.g., fucoxanthin (PSC) for diatoms, peridinin (PPC) for certain dinoflagellates, alloxanthin (PPC) for cryptophytes, zeaxanthin (PPC) for prokaryotes (e.g. cyanobacteria), and the degradation products of Chl a, namely, divinyl Chl a and divinyl-Chl b for prochlorophyte (Jeffrey and Vest, 1997). High-Performance Liquid Chromatography (HPLC) which can efficiently detect and quantify several chemo-taxonomically significant chlorophylls and carotenoids, when coupled with these taxa-specific pigment ratios, allow phytoplankton taxonomic composition to be quantified based on a pigment concentration diagnostic procedures such as CHEMTAX (Mackey et al., 1996). Furthermore, phytoplankton pigments with distinct absorption characteristics strongly influence the light absorption by phytoplankton (Bidigare et al., 1990; Ciotti et al., 2002; Bricaud et al., 2004). As such, phytoplankton absorption spectra has been used to infer underlying pigments and also phytoplankton taxonomy by Gaussian-decomposition of (Hoepffner and Sathyendranath, 1991; Lohrenz et al., 2003; Ficek et al., 2004; Chase et al., 2013; Moisan et al., 2013; Wang et al., 2016; Moisan et al., 2017). More importantly, phytoplankton optical properties (absorption and backscattering) bearing the imprints of different pigments and cell-size, are important contributors to reflectance in a waterbody (Gordon et al., 1988). Morel and Prieur, (1977) first reported the feasibility of calculating the phytoplankton absorption coefficients and other inherent optical properties (IOPs) from measured subsurface irradiance reflectance based on the simplified radiative transfer equation. Improvements in semi-analytical inversion algorithms to derive IOPs from in-situ and remotely sensed reflectance spectra have been reported (Roesler and Perry, 1995; Hoge and Lyon, 1996; Lee et al., 1996; Garver and Siegel, 1997; Carder et al., 1999; Maritorena et al., 2002; Roesler and Boss, 2003; Chase et al., 2017). Roesler et al. (2003) further modified an earlier IOP inversion algorithm used in Roesler and Perry, (1995) by adding a set of 5 species-specific phytoplankton absorption spectra, and derived phytoplankton taxonomic composition from the field measured remote sensing reflectance.

Phytoplankton pigment composition varies not only between taxonomic groups but also with photo-physiological state of cells and environmental stress (e.g., light, nutrients, temperature, salinity, turbulence and stratification) (Suggett et al., 2009). The photosynthetic pigment field is an important factor influencing the magnitude of fluorescence emitted by phytoplankton, with active fluorometry commonly used to obtain estimates of phytoplankton biomass (D'Sa et al., 1997). Advanced active fluorometry termed as fast repetition rate (FRR; (Kolber et al., 1998)) and analogous techniques such as the fluorescence induction and relaxation (FIRe; Suggett et al., 2008) allows for the simultaneous measurements of the maximum PSII photochemical efficiency (F_V/F_M; where F_m and F_o is maximum and minimum fluorescence yield and F_v is variable fluorescence obtained by subtracting F_o from F_m) and the effective absorption cross section (σ_{PSII}) of a phytoplankton population; these have been used as diagnostic indicators for the rapid assessment of phytoplankton health and photo-physiological state linked to environmental stressors. Considerable effort has been invested to achieve a deeper understanding of the impacts of environmental factors and phytoplankton taxonomy on photosynthetic performance of natural communities from field and laboratory fluorescence measurements (Kolber et al., 1988; Geider et al., 1993; Schitüter et al., 1997; Behrenfeld and Kolber, 1999; D'Sa and Lohrenz, 1999;

Holmboe et al., 1999; Moore et al., 2003). Furthermore, knowledge of photo-physiological responses of phytoplankton in combination with information on phytoplankton taxonomic composition could provide additional insights on regional environmental conditions.

Synoptic mapping of aquatic ecosystems using satellite remote sensing has revolutionized our understanding of phytoplankton dynamics at various spatial and temporal scales in response to environmental variabilities and climate change. It has also provided greater understanding of biological response to large events such as hurricanes in oceanic and coastal waters (Babin et al. 2004; Acker et al. 2009; D'Sa 2014; Farfan et al. 2014; Hu and Feng, 2016). Although the primary focus of ocean color sensors has been to determine the Chl a concentration and related estimates of phytoplankton primary production (Mitchell, 1994; Behrenfeld and Falkowski, 1997), more recently, several approaches have been developed based on phytoplankton optical signatures to derive spatial distributions of phytoplankton functional types (PFTs) (Alvain et al., 2005; Nair et al., 2008; Hirata et al., 2011), phytoplankton size classification (Ciotti et al., 2002; Hirata et al., 2008; Brewin et al., 2010; Devred et al., 2011), and phytoplankton accessory pigments (Pan et al., 2010; Pan et al., 2011; Moisan et al., 2013; Moisan et al., 2017; Sun et al., 2017). The basis of these satellite-based remote sensing algorithms have relied on distinct spectral contributions from phytoplankton community composition (e.g., taxonomy, size structure) to remote sensing reflectance (R_{rs}, sr^{-1}); however, these studies have all been confined to open ocean and shelf waters. In contrast, satellite studies of phytoplankton pigments have been limited in the optically complex estuarine waters where the influence from wetlands, rivers, and coastal ocean make phytoplankton communities highly variable and complex.

In this study, field bio-optical measurements and ocean color remote sensing data (Sentinel-3A OLCI) acquired in Galveston Bay, a shallow estuary along the Gulf coast (Texas, USA; Fig. 1), are used to investigate the spatial distribution of phytoplankton pigments, taxonomic composition, and their photo-physiological state following the extreme flooding of the Houston Metropolitan and surrounding areas due to Hurricane Harvey and the consequent biological impact of the floodwater discharge into the bay. The paper is organized as follows: section 2 describes the field data acquisition and laboratory processing, section 3 presents the algorithms and methods used to distinguish phytoplankton groups, retrieve spatial distribution of pigments, and calibrate phytoplankton physiological parameters. Results and discussions (section 4 and 5), and summary (section 6) addresses the main contributions and findings of this paper.

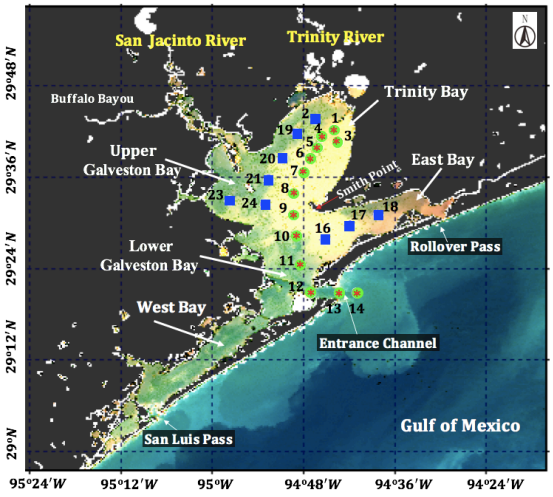

Figure 1. Sentinel-3A OLCI RGB image (October 29, 2017) with locations of sampling sites in Galveston Bay acquired on September 29 (red asterisk), October 29 (green circles) and October 30 (blue solid squares), 2017, respectively.

2. Data and Methods

2.1 Study area

Galveston Bay (GB), a shallow water estuary (~2.1 m average depth), encompasses two major sub-estuaries: San Jacinto Estuary (also divided as Upper GB and Lower GB), and Trinity Estuary (Trinity Bay) (Fig. 1). It is located adjacent to the heavily urbanized and industrialized metropolitan areas of Houston, Texas (Dorado et al., 2015). A deep (~14 m) narrow Houston Ship Channel connects the bay to the northern Gulf of Mexico (nGoM) through a narrow entrance, the Bolivar Roads Pass. Tidal exchange between GB and the nGoM occurs through the entrance channel with diurnal tides ranging from ~0.15 to ~0.5 m. The major freshwater sources to GB are the Trinity River (55%), the San Jacinto River (16%), and Buffalo Bayou (12%) (Guthrie et al., 2012). The San Jacinto River was frequently observed to transport greater amounts of dissolved nutrients into GB than the Trinity River (Quigg, 2011); however, the negative relationship between nitrate concentrations and salinity observed in the mid-bay area (adjacent to Smith Point) (Santschi, 1995), indicated Trinity River to be a major source of nitrate in GB. The catastrophic flooding of Houston and surrounding areas associated with Hurricane Harvey resulted in strong freshwater inflows into GB from the San Jacinto River (>3300 m^3s^{-1}; USGS 08067650) on August 29, 2017 and the Trinity River (>2500 m^3s^{-1}; USGS 08066500 site at Romayor, Texas) on August 30, 2017, respectively. Although the discharge from the two rivers in the upstream returned to normal conditions (~50–120 m^3s^{-1}) in about 2 weeks after the Hurricane passage, salinity remained low for over a month following the hurricane passage (D'Sa et al., 2018).

2.2 Sampling and Data Collection

Surface water samples were collected at a total of 34 stations during two surveys on September 29 and October 29–30, 2017 (Fig. 1). Samples at stations 1 to 14 (red asterisk on top of green circle; Fig. 1) along the Trinity River transect were collected repeatedly on September 29 and October 29, 2017, respectively. Additional 9 sampling sites (blue squares; Fig. 1) around the upper bay and in the East Bay were sampled on October 30, 2017. The surface water samples were stored in coolers and filtered on the same day. The filter pads were immediately frozen and stored in liquid nitrogen for laboratory absorption spectroscopic and HPLC measurements of the samples. An optical package equipped with a conductivity-temperature-depth recorder (Sea-Bird SBE) and a Fluorescence Induction and Relaxation System (FIRe; Satlantic Inc) was used to obtain profiles of salinity, temperature, pressure, and phytoplankton physiological parameters (F_V/F_M and σ_{PSII}). Measurements of backscattering were also made at each station using the WETLabs VSF-3 (470, 530, 670 nm) backscattering sensor (D'Sa et al. 2006). Included in the optical package was also a hyperspectral downwelling spectral irradiance meter (HyperOCR, Satlantic). The irradiance data from HyperOCR were processed using Prosoft 7.7.14 and the photosynthetically Active Radiation (PAR) were estimated from the irradiance measurements. The above-water reflectance measurements were collected using a GER 1500 512iHR spectroradiometer in the 350-1050 nm spectral range. At each station, sky radiance, plate radiance, and water radiance were recorded (each repeated three times) and processed to obtain above-water remote sensing reflectance (Joshi et al., 2017). A total of 43 Sentinel-3A OLCI full resolution mode, cloud free level-1 images were obtained over GB between August 01, 2016-December 01, 2017 from the European Organization for Meteorological Satellites (EUMESAT) website and pre-processed using Sentinel-3 Toolbox Kit Module (S3TBX) version 5.0.1 in Sentinel Application Platform (SNAP). These Sentinel-3A OLCI data were further atmospherically corrected to obtain remote sensing reflectance ($R_{rs\ OLCI}$, sr^{-1}) using Case-2 Regional Coast Color (C2RCC) module version 0.15 (Doerffer and Schiller, 2007). River discharge information during August, 2016-December, 2017 was downloaded from the USGS Water Data (USGS) for Trinity River at Romayor, Texas (USGS 08066500) and the west flank of the San Jacinto River (USGS 08067650). Individual pictures of microplankton (10 to 150 µm) recorded by an Imaging

FlowCytobot (IFCB) located at the entrance to Galveston Bay were downloaded (http://dq-cytobot-pc.tamug.edu/tamugifcb) for pigment validation.

2.3 Absorption Spectroscopy

Surface water samples were filtered through 0.2-µm nuclepore membrane filters and the colored dissolved organic matter (CDOM) absorbance (A_{CDOM}) were obtained using a 1-cm path length quartz cuvette on a Perkin Elmer Lambda-850 UV/VIS spectrophotometer equipped with an integrating sphere. The Quantitative Filter Technique (QFT) with 0.7-µm GF/F filters were used to measure absorbance of particles (A_{total}) and non-algal particles (A_{NAP}) inside an integrating sphere at 1 nm intervals from 300 to 800 nm. The absorption coefficients of CDOM (a_{CDOM}), NAP (a_{NAP}), particles (a_{total}) and phytoplankton (a_{PHY}) were calculated using the following equations:

$$a_{CDOM}(\lambda) = 2.303 \times \frac{A_{CDOM}(\lambda)}{L} \quad \ldots\ldots (1)$$

where L is the path length in meters. The a_{CDOM} were corrected for scattering, temperature, and baseline drift by subtracting an average value of absorption between 700-750 nm for each spectrum (Joshi and D'Sa, 2015).

$$a_{total}(\lambda) = 2.303 \times \frac{A_{total}(\lambda)}{V_{filtered}/S_{filter}} \quad \ldots\ldots (2)$$

$$a_{NAP}(\lambda) = 2.303 \times \frac{A_{NAP}(\lambda)}{V_{filtered}/S_{filter}} \quad \ldots\ldots (3)$$

$$a_{PHY}(\lambda) = a_{total} - a_{NAP} \quad \ldots\ldots (4)$$

where $V_{filtered}$ is the filtered volume of sample, S_{filter} is the area of filter pads and the path length correction for filter pad was applied according to (Stramski et al., 2015).

2.4 Pigment Absorption Spectra

The water samples were filtered with 0.7-µm GF/F filter. The filter pads were stored in liquid nitrogen until transferred into 30 ml vials containing 10 ml cold 96% ethanol (Ritchie, 2006). The vials were spun evenly to ensure full exposure of the filter pad to the ethanol and then kept in the refrigerator (in the dark) overnight. The pigment solutions at room-temperature were poured off from vials into 1 cm cuvette and measured on a Perkin Elmer Lambda-850 UV/VIS spectrophotometer to obtain pigment absorbance spectra (A_{pig}), while, 90% ethanol was used as a blank (Thrane et al., 2015). The total absorption coefficients of pigments $a_{pig}(\lambda)$ were calculated as follow:

$$a_{pig}(\lambda) = 2.303 \times \frac{A_{pig}(\lambda)}{L} \times \left(\frac{V_{ethanol}}{V_{filtered}}\right) \quad \ldots\ldots (5)$$

where L is the path length in meters, $V_{ethanol}$ is the volume of ethanol, and $V_{filtered}$ is the filtered volume of the water samples.

2.5 HPLC Measurements

Water samples were filtered through 0.7-µm GF/F filters and immediately frozen in liquid nitrogen for HPLC analysis using the methods reported by Barlow et al. (1997). The detected pigments along with their abbreviations are listed in Table 1. Diagnostic biomarker pigments are marked in bold letters (Table 1).

Table 1. Pigments information acquired from HPLC samples in Galveston Bay.

Variable	Primary Pigment (PPig)	Calculation
	Chlorophylls	
[TChl a]	Total chlorophyll a (TChl a)	[Chlide a]+[DVChl a]+[Chl a]
[TChl b]	Total chlorophyll b (TChl b)	[DVChl b]+**[Chl b]**
[TChl c]	Total chlorophyll c (TChl c)	[Chl c_1]+[Chl c_2]+[Chl c_3]
	Carotenoids	
[Caro]	Carotenes†	[ββ-Car]+[βε-Car]
[Allo]	**Alloxanthin**	
[Buta]	**19'-Butanoyloxyfucoxanthin**	
[Diadino]	Diadinoxanthin	
[Diato]	Diatoxanthin	
[Fuco]	**Fucoxanthin**	
[Hexa]	**19'-Hexanoyloxyfucoxanthin**	
[Peri]	**Peridinin**	
[Zea]	**Zeaxanthin**	
[Neo]	Neoxanthin	
[Lut]	Lutein	
[Viola]	Violaxanthin	
[Pras]	Prasinoxanthin	
[Anthera]	Antheraxanthin	
Note: (1) [Chl b], [Allo], [Fuco], [Peri], [Zea], [Buta] and [Hexa] are considered as diagnostic pigments for PFTs (Moisan et al., 2017).		
Variable	Pigment Sum	Calculation
[TChl]	Total Chlorophyll (TChl)	[TChl a]+[TChl b]+[TChl c]
[PPC]	Photoprotective Carotenoids (PPC)	[Allo]+[Diadino]+[Diato]+[Zea]+[Caro]+[Viola]
[PSC]	Photosynthetic Carotenoids (PSC)	[Buta]+[Fuco]+[Hexa]+[Peri]+[Lut]+[Pras]
[PSP]	Photosynthetic Pigments (PSP)	[PSC]+[TChl]
[AP]	Total Accessory Pigments (AP)	[PPC]+[PSC]+[TChl b]+[TChl c]
[TP]	Total Pigments (TP)	[AP+[TChl a]
[DP]	Total Diagnostic Pigments (DP)	[PSC]+[Allo]+[Zea]+[T Chl b]

2.6 FIRe Measurements

An in-situ Fluorescence Induction and Relaxation System (FIRe, Satlantic Inc.) was used to characterize phytoplankton photosynthetic physiology during the two surveys in GB. The FIRe is based on illuminating a sample with an intense flash of light to instantaneously saturate the reaction centers of photosystem II (PSII); under these light conditions, reaction centers do not accept electrons and most of the absorbed light energy is dissipated as fluorescence. The fundamental parameter measured by FIRe is

fluorescence yield F(t), which is the emitted fluorescence divided by the irradiance intensity (no unit). In contrast to strong flashes, dark adaption enables all reaction centers of PSII to be open with least fluorescence emitted, thus, resulting in minimal fluorescence yield (F_o). Maximum fluorescence yield (F_m) can be obtained after sufficient irradiation when all reaction centers are closed. Maximum photochemical efficiency, which quantify the potential of converting light to chemical energy for the PSII reaction centers (Moore et al., 2006), was calculated as (F_m - F_o)/ F_m = F_v / F_m. The functional absorption cross section σ_{PSII} ($Å^2 quantum^{-1}$) measures the capability of reaction centers to absorb light from the ambient environment. The FIRe was deployed at a slow descent rate, with 12 and 20 vertical profiles obtained during the first and second surveys, respectively. All measurements were programmed using standard protocols of single saturating turn-over (ST) flash saturation of PSII (Kolber et al., 1998). Flashes were generated from highly uniform blue LEDs at 455 nm with approximately 30 nm half-bandwidth. Chl a fluorescence was stimulated using saturating sequence of 80 1.1 µs flashes applied at 1 µs intervals, 8 sequences were averaged per acquisition, and the fluorescence signal was detected at 668 nm. All data were processed using standard FIReCom software (Satlantic). In addition, samples of 0.2-µm filtered sea water at each station were used as 'blank' to remove the background fluorescence signals (Cullen and Davis, 2003); in this step, the fluorescence from the filtered samples (without phytoplankton) were subtracted from in-situ fluorescence signals to get more accurate values of F_v/F_m.

2.7 Retrieving Phytoplankton Groups from above-water R_{rs}

A fundamental relationship that links sub-surface remote-sensing reflectance (r_{rs}) and the IOPs was expressed using a quadratic function developed by (Gordon et al., 1988):

$$r_{rs} = g_1 * u(\lambda) + g_2 * u(\lambda)^2;\ u(\lambda) = \frac{b_b}{a_{total}+b_b} \quad \ldots\ldots (6)$$

where, the parameters g_1 (~0.0788) and g_2 (~0.2379) are values for turbid estuarine waters (Joshi and D'Sa, 2018); r_{rs} is the sub-surface remote sensing reflectance that were obtained from above-water remote sensing reflectance (R_{rs}) using (Lee et al., 2002):

$$r_{rs} = \frac{R_{rs}}{0.52+1.7 \times R_{rs}} \quad \ldots\ldots (7)$$

The total backscattering coefficient b_b is comprised of water (b_{bw}) and particulates including both organic and inorganic particles (b_{bp}), while the total absorption coefficients (a_{total}) can be further separated into four sub-constituents (Roesler and Perry, 1995) as indicated by:

$$b_b = b_{bw} + b_{bp};\ \ a_{total} = a_w + a_{phy} + a_{CDOM} + a_{NAP} \quad \ldots\ldots (8)$$

where a_w, a_{phy}, a_{CDOM}, and a_{NAP} represent the absorption coefficients of pure water, phytoplankton, colored dissolved organic matter and non-algal particles, respectively.

The IOP inversion algorithm for retrieving IOPs from R_{rs} require known spectral shape (eigenvector) of each component in Eq. (8) to estimate the magnitude (eigenvalues) of each component (Table 2). The spectral shape can be adjusted by changing the values of slope based on characteristics of the study area. It is worth noting that a single averaged phytoplankton eigenvector does not provide species information whereas a set of several species-specific phytoplankton eigenvectors allow estimates of species composition. IOPs inversion algorithm applied in this study makes use of mass-specific phytoplankton absorption spectra of 10 groups namely, dinoflagellate, diatom, chlorophyte, cryptophyte, haptophyte, prochlorophyte, raphidophyte, rhodophyte, red cyanobacteria and blue cyanobacteria; these were obtained

from Dierssen et al. (2006) and Dutkiewicz et al. (2015) as eigen vectors rather than using one average $a_{phy}(\lambda)$ spectrum. Subsequently, the inversion algorithm iterates repeatedly to minimize the difference between modeled R_{rs} and in-situ measured R_{rs} (R_{rs_insitu}) until a best fit is achieved while allowing for alterations of all parameters listed in Table 2 (Chase et al., 2017). The absolute percent errors between modeled and measured values of R_{rs}, a_{phy}, a_{CDOM}, a_{NAP} and b_{bp} were calculated as:

$$\%\text{error} = \left|\frac{X_{\text{modeled}} - X_{\text{measured}}}{X_{\text{measured}}}\right| \times 100 \quad \ldots\ldots (9)$$

Table 2. Parameters and eigenvectors used in the semi-analytical inversion algorithm.

Parameter	Equation	Slope	Eigenvalue
$a_{CDOM}(\lambda)$	$a_{CDOM}(\lambda) = M_{CDOM} \times \exp^{-S_{CDOM} \times (\lambda - \lambda_0)}$; $\lambda_0 = 443$	S_{CDOM}	M_{CDOM}
$a_{NAP}(\lambda)$	$a_{NAP}(\lambda) = M_{NAP} \times \exp^{-S_{NAP} \times (\lambda - \lambda_0)}$; $\lambda_0 = 443$	S_{NAP}	M_{NAP}
$a_{phy}(\lambda)$	$a_{phy}(\lambda) = \sum \text{Chl } a_i \times a^*_{phi}$; a^*_{phi} is the spectral shape of each phytoplankton group.		$\text{Chl } a_i$
$b_{bp}(\lambda)$	$b_{bp}(\lambda) = B_{bp} \times (\lambda_0/\lambda)^{S_{bp}}$; $\lambda_0 = 443$	S_{bp}	B_{bp}
Note: $a^*_{phi}(\lambda)$ for 10 different groups of phytoplankton used in this study were extracted from (Dierssen et al., 2006) and Dutkiewicz et al., (2015).			

2.8 Retrieving Pigments from Sentinel 3-OLCI R_{rs}

2.8.1 Reconstruction of Pigment Absorption Spectrum by Multiple Linear Regression

Total pigment absorption spectra $a_{pig}(\lambda)$ obtained during both surveys (Eq. 5), were modeled as a third order function of HPLC measured Chl a ($\text{Chl a}_{\text{HPLC}}$) concentration at each station as (Moisan et al., 2017):

$$a_{pig}(\lambda) = C_3 \times (\text{Chl a\_}_{\text{HPLC}})^3 + C_2 \times (\text{Chl a\_}_{\text{HPLC}})^2 + C_1 \times \text{Chl a\_}_{\text{HPLC}} + C_0 \quad \ldots\ldots (11)$$

where vector coefficient C=[C_3, C_2, C_1, C_0], are wavelength-dependent coefficients that range from 400 to 700 nm at 1 nm interval; these were further applied to Sentinel-3A OLCI Chl a to calculate a_{pig_OLCI} at each pixel as:

$$a_{pig\_OLCI}(\lambda) = C_3 \times (\text{Chl a\_}_{\text{OLCI}})^3 + C_2 \times (\text{Chl a\_}_{\text{OLCI}})^2 + C_1 \times \text{Chl a\_}_{\text{OLCI}} + C_0 \quad \ldots\ldots (12)$$

where $\text{Chl a\_}_{\text{OLCI}}$ is Sentinel-3A OLCI derived Chl a concentration (259×224 pixels); the obtained image represents the value of a_{pig_OLCI} at a certain wavelength and 301 images of a_{pig_OLCI} can be obtained in the 400-700 nm wavelength range at 1 nm interval.

2.8.2 Satellite Retrieval of Pigments using Non-Negative Least Square (NNLS) Inversion Model

The a_{pig_OLCI} is a mixture of n pigments with known absorption spectra $a_i(\lambda)$, $i = 1,2,\ldots,n$ at wavelength λ (nm); thus, $a_{pig\_OLCI}(\lambda)$ can be considered as a weighted sum of individual component spectrum (Thrane et al., 2015) at each image point as:

$$a_{pig\_OLCI}(\lambda) = x_1 \times a_1(\lambda) + x_2 \times a_2(\lambda) + \cdots x_n \times a_n(\lambda) \quad \ldots\ldots (13)$$

where $A(\lambda) = [a_1(\lambda), a_2(\lambda), \ldots a_n(\lambda)]$ represent the mass-specific spectra of 16 pigments (Chl a, Chl b, Chl c_1, Chl c_2, pheophytin-a, pheophytin-b, peridinin, fucoxanthin, neoxanthin, lutein, violaxanthin, alloxanthin, diadinoxanthin, diatoxanthin, zeaxanthin, and β-carotenoid), which are the in-vitro pigment absorption spectra over pigment concentrations and can be extracted from supplementary R scripts of Thrane et al. (2015). The vector coefficient $X = [x_1, x_2, \ldots x_n]$ correspond to the concentrations (μg L^{-1}) of these distinct pigments; note that X cannot be negative, therefore, non-negative least squares (NNLS) was used to guarantee positive solutions of X (Moisan et al., 2013; Thrane et al., 2015). Eq. 13 can be further expressed as:

$$\begin{bmatrix} a_{pig}(400)_{OLCI} \\ a_{pig}(401)_{OLCI} \\ \vdots \\ a_{pig}(700)_{OLCI} \end{bmatrix} = \begin{bmatrix} x_1 \\ x_2 \\ \vdots \\ x_n \end{bmatrix} \times \begin{bmatrix} a_1(400), a_2(400), \ldots a_n(400) \\ a_1(401), a_2(401), \ldots a_n(401) \\ \vdots \\ a_1(700), a_2(700), \ldots a_n(700) \end{bmatrix} \quad \ldots\ldots (14)$$

2.9 Processing Approach

Sentinel 3A-OLCI pigment maps were generated using the processing pathway 1 (Fig. 2) that includes the following: 1) developing empirical relationships between HPLC-measured Chl a and R_{rs_insitu} band ratio for Sentinel 3A-OLCI band 9 (673 nm) and band 11 (709 nm) to generate Sentinel 3A-OLCI Chl a maps, 2) converting Chl a concentration to $a_{pig\_OLCI}(\lambda)$ maps, and subsequently decomposing $a_{pig\_OLCI}(\lambda)$ into individual pigment spectra to generate phytoplankton pigment maps for GB. In processing pathway 2, phytoplankton taxonomic composition at each sampling station was obtained from a 10-species IOP inversion model, which take R_{rs_insitu} as input and estimates Chl a concentration of each phytoplankton group (Fig. 2). Finally, CDOM-corrected FIRe measurements of F_v/F_m and σ_{PSII} were combined with phytoplankton taxonomy to assess photosynthetic physiology of different phytoplankton groups.

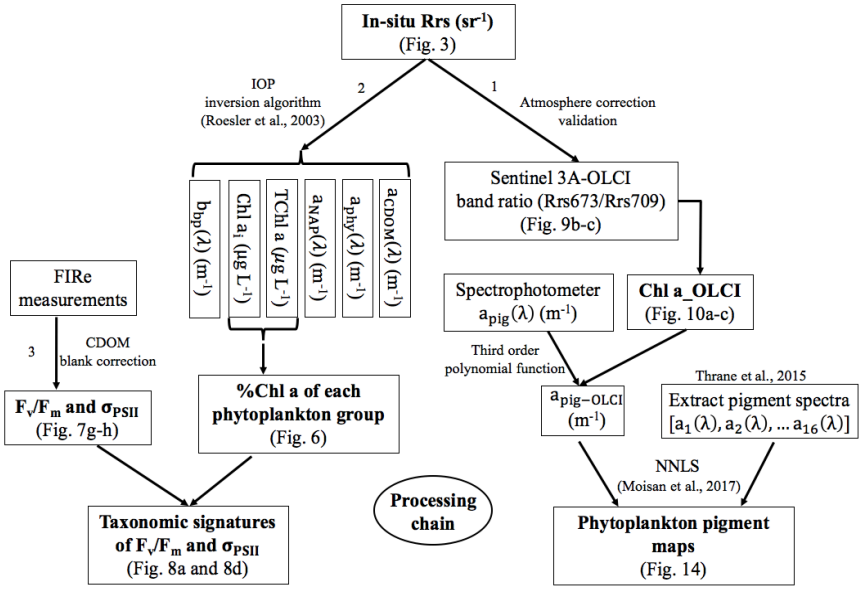

Figure 2. Flowchart showing the three processing steps for: (1) retrieving pigments spatial distribution maps from OLCI, (2) distinguishing phytoplankton groups, and (3) assessing phytoplankton physiological

parameters and their linkages to taxonomic groups.

3. Results

3.1 Phytoplankton Taxonomy and Physiological State from Field Observations

3.1.1 Measurements of Above Water Remote Sensing Reflectance

Above-water remote sensing reflectances (R_{rs_insitu}) from the two surveys (Fig. 3) reflect the influence of the absorbing and scattering features of water constituents. Low reflectance (~675 nm) caused by Chl a red light absorption and maximum reflectance at green wavelength (~550 nm) were observed. Obvious dips at ~625 nm versus reflectance peaks ~650 nm were observed in spectra during both surveys, which could be attributed to cyanobacteria modulation of the spectra (Hu et al., 2010). The reflectance peak around 690–700 nm was obvious at most sampling sites except at stations 13 and 14 adjacent to the nGOM and were likely due to the effect of Chl a fluorescence (Gitelson, 1992; Gilerson et al., 2010). The peak position at stations with lower Chl a concentration (~5 µg L^{-1}) were observed at 690-693 nm; however, the peaks shifted to longer wavelengths of 705 and 710 nm for station 23 and 19 with extremely high Chl a concentrations of ~31 and 50 µg L^{-1}, respectively (Fig. 3).

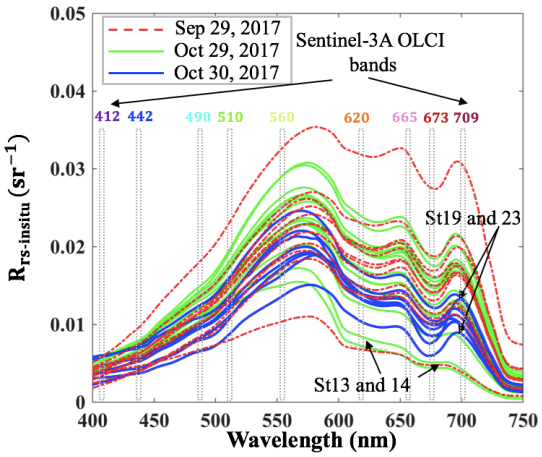

Figure 3. R_{rs_insitu} spectra at stations in GB on September 29, and October 29-30, 2017; vertical bars represent Sentinel-3A OLCI spectral bands.

3.1.2 Performance of IOP Inversion Algorithm

The IOP inversion algorithm was applied to R_{rs_insitu} data (Fig. 3) obtained during the two surveys in GB. The mean errors for modeled a_{CDOM}, a_{NAP}, a_{phy} and b_{bp_470} at all wavelengths for the 34 stations were 5.86%, 6.83%, 12.19% and 10.79%, respectively (Table 3). A total of 8 phytoplankton groups (dinoflagellate, diatom, chlorophyte, cryptophyte, haptophyte, prochlorophyte, raphidophyte, and blue cyanobacteria) were spectrally detected from IOP inversion algorithm. The sum of 8 eigenvalues of Chl_i (Table 2) represents the modeled total Chl a (TChl a_mod) of the whole phytoplankton community. The TChl a_mod is better correlated with HPLC-measured total Chl a (TChl a_HPLC) for survey 2 (green circle; Fig. 4a) with $R^2 \sim 0.92$, compared to survey 1 (red color; Fig. 4a). In addition, the TChl a_mod appear to be slightly higher than TChl a_HPLC for survey 2. The modeled a_{CDOM} (a_{CDOM_mod}) are in close agreement with spectrophotometrically measured a_{CDOM} at 412 nm (Fig. 4b), with a_{CDOM} obtained on September 29, 2017 much higher than that on October 29-30, 2017. The modeled b_{bp} (b_{bp_mod}) are well correlated with in-situ b_{bp} (b_{bp_insitu}) at 470 nm (Fig. 4c) with higher R^2 (0.81) observed on September 29, 2017. In addition, both

modeled and field-measured b_{bp} showed stronger backscattering at most stations on September 29, 2017 than those on October 29-30, 2017.

Table 3. Error statistics over all wavelengths and sampling stations (N=301×34=10234; 12 and 22 stations on Sep 29 and Oct 29-30, 2017) from semi-analytical IOP inversion algorithm.

Parameter	Min. error (%)	Max. error (%)	Mean error (%)	R^2(Sep)	R^2(Oct)
$R_{rs}\ \lambda \in [400,700]$	0.005	40.12	18.71	0.90	0.89
$a_{CDOM}(\lambda),\ \lambda \in [400,700]$	0.042	11.20	5.86	0.92	0.94
$a_{NAP}(\lambda),\ \lambda \in [400,700]$	0.001	11.46	6.73	0.90	0.91
$a_{PHY}(\lambda),\ \lambda \in [400,700]$	0.001	36.42	12.19	0.84	0.85
$b_{bp}(\lambda),\ \lambda = 470$ nm	0.057	40.22	10.79	0.81	0.43

The Chl a percentage (%Chl a), which is Chl_i/TChl a, were also compared with diagnostic pigment percentage (%DP), which is specific DP for each phytoplankton group over the sum of DP (∑ DP). The DP for diatom (fucoxanthin), dinoflagellate (peridinin), cryptophytes (alloxanthin), chlorophyte (Chl b), haptophyte (19'-hexanoyloxyfucoxanthin), and cyanobacteria (zeaxanthin) referred in (Moisan et al., 2017) were used in this study. The R^2 between %Chl a and %DP for different phytoplankton groups range from 0.15 to 0.81 (Fig. 4). The %Chl a of cryptophyte is between 5%-42% and well correlated with alloxanthin/∑ DP (R^2~0.62-0.72; Fig. 4d) for both surveys. In addition, the cryptophyte %Chl a at station 19 and 23 on October 30, 2017 was highest (~40%) in coincidence with the highest value of alloxanthin/ ∑ DP (Fig. 4d). Furthermore, relationship between chlorophyte %Chl a and Chl b/∑ DP (R^2~0.55; Fig. 4e) showed that chlorophyte during survey 1 contributed higher fraction to the whole phytoplankton community compared to survey 2. The %Chl a of cyanobacteria highly correlated with zeaxanthin/ ∑ DP with R^2 larger than 0.7 (Fig. 4f) for both surveys. Low %Chl a of dinoflagellate in coincidence with low peridinin/ ∑ DP (R^2~0.78) were observed at stations along the transect, however, increased contribution of dinoflagellate appeared adjacent to the entrance during both surveys (Fig. 4g).

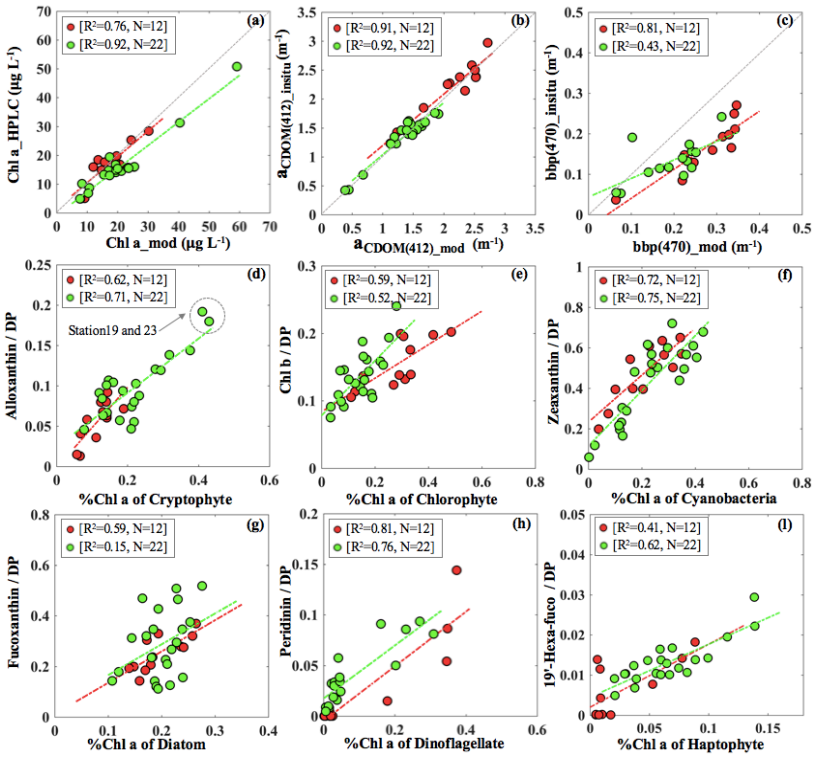

Figure 4. (a) Validation of TChl a_mod via HPLC-measured TChl a; individual %Chl a of each detected taxa versus corresponding %DP shown with (d) cryptophyte, (e) chlorophyte, (f) cyanobacteria, (g) diatom, (h) dinoflagellate, and (l) haptophyte; red and green dots indicate the samples on September 29 and October 29-30, 2017, respectively. Comparison between in-situ measurements and modeled results with (b) $a_{CDOM}(412)$ and (c) $b_{bp}(470)$.

3.1.3 Variations in Phytoplankton Community Structure

Reconstruction of the phytoplankton absorption coefficients spectra revealed variations in phytoplankton community structure (Fig. 5) even several weeks after Hurricane Harvey. The modeled a_{phy} spectra (a_{phy_mod}) at stations 6, 13, 17 and 19 (Fig. 5a-f) yielded spatiotemporal differences of phytoplankton taxonomic composition in GB. The strong absorption peak around 625 nm induced by cyanobacteria was observed at most of the stations for both modeled results and in-situ measurements (Fig. 5a, 5c and 5e) except at stations adjacent to the entrance (Fig. 5b and d). The a_{phy_mod} at station 6 was primarily dominated by group of cyanobacteria (blue line) and chlorophyte (green line) on September 29, 2017 (Fig. 5a); in contrast, the spectrum of chlorophyte contributed very little at station 6 on October 29, 2017 (green line; Fig. 5c). Furthermore, the shape of spectra for samples obtained at station 13 showed strong dinoflagellate-modulation versus extremely low cyanobacteria contribution during survey 1 (red line; Fig. 5b). However, small-size group like haptophyte and prochlorophyte displayed increasing proportions at station 13 on October 29, 2017 (Fig. 5d). Station 17 in the East Bay was dominated by cyanobacteria (blue line; Fig. 5e) and cryptophyte (pink line; Fig. 5e) absorption spectra, whereas, on October 30, 2017, the main spectral features at station 19 in the upper GB was from cryptophyte (pink line) and chlorophyte (green line; Fig. 5f).

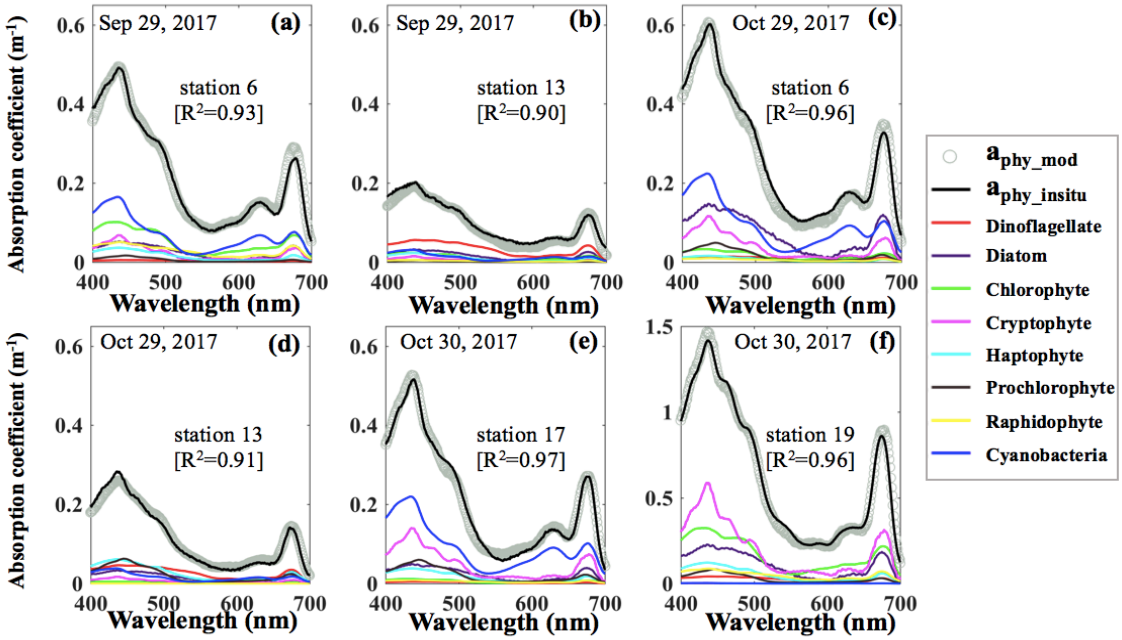

Figure 5. Reconstruction of phytoplankton absorption coefficients spectra at station 6 **(a)** and 13 **(b)** on September 29, 2017, at station 6 **(c)** and 13 **(d)** on October 29, 2017 and at 17**(e)**, and 19 **(f)** on October 30, 2017 based on the mass specific absorption spectra of different phytoplankton groups including diatom, chlorophyte, dinoflagellate, cryptophyte, cyanobacteria (blue), haptophyte, prochlorophyte and raphidophyte presented using different colors.

The corresponding taxa-specific %Chl a derived from IOPs inversion algorithm for the two surveys on September 29 and October 29-30, 2017 are shown in Figure 6a and 6b, respectively. Cyanobacteria (blue

bars) and chlorophyte (green bars) constituted over 55% of the phytoplankton communities during survey 1 (September 29, 2017; Fig. 6a). In addition, chlorophyte, known to proliferate in freshwater environments, showed higher fraction than that observed in survey 2 (green color; Fig. 6). Further, chlorophyte together with diatoms (purple color; Fig. 6a) accounted for ~ 60% of TChl a_{mod} at many stations (e.g., station 7, 8 and 9) with a well-mixed water column (inferred from salinity profiles; not shown) on September 29, 2017. Cryptophyte, haptophyte and raphidophyte became a minor component of the community and accounted in total to ~25% of TChl a_{mod} (Fig. 6a). Furthermore, contribution by dinoflagellate group to TChl a_{mod} was low inside the bay, but showed increasing %Chl a (~30%) in higher salinity waters adjacent to the nGOM (red color; Fig. 6a). Cyanobacteria (blue color; Fig. 7) exhibited a slightly elevated percentage during survey 2 (~60 days after hurricane passage, October 29-30, 2017) and were quite abundant at station 16, 17 and 18 in East Bay where the water was calm and stratified as observed from salinity profiles. In addition, cyanobacteria were not prevailing adjacent to the nGOM (Station 12, 13 and 14) and close to San Jacinto (station 19, 20, 21, 23 and 24), where cryptophyte (pink color) and chlorophyte (green color) showed dominance (Fig. 6b). The %Chl a of chlorophyte obtained at stations along the Trinity River transect decreased by ~10% on October 29-30, 2017 compared to that on September 29, 2017. Small size groups like haptophyte and prochlorophyte increased on October 29-30, 2017 and were more abundant adjacent to the nGOM, accounting for more than 25% of the TChl a_{mod}.

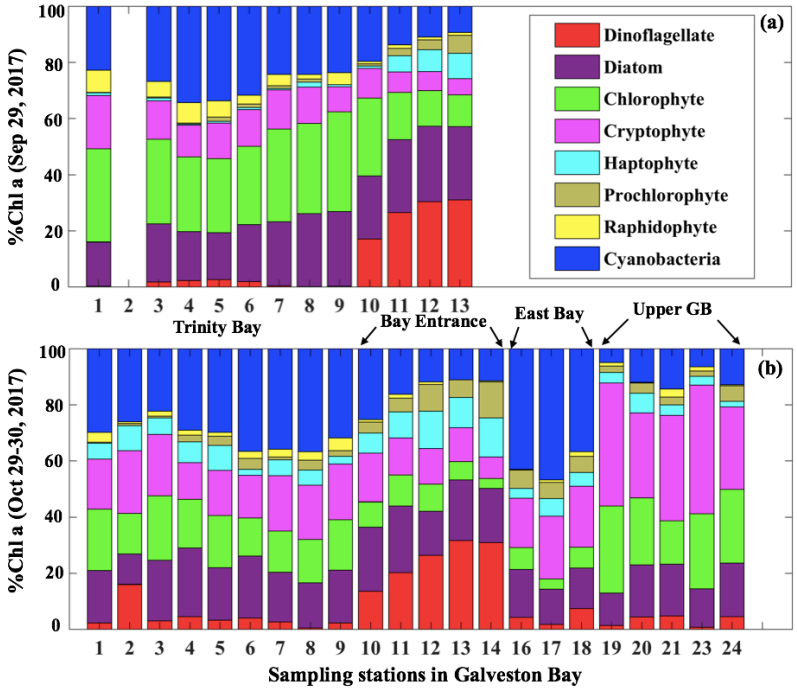

Figure 6. Phytoplankton taxonomic compositions detected from IOP inversion algorithm on September 29 and October 29-30, 2017 in Galveston Bay; phytoplankton groups are represented in different colors as shown in the legend.

3.1.4 Environmental Conditions and Physiological State of Phytoplankton Community

The surface salinity presented a pronounced seaward increasing gradient along the transect (station 3-14) during both the surveys (Fig. 7a) with primarily lower salinity throughout the bay during survey 1 in comparison to survey 2, which indicated the freshening impact was still ongoing even 4 weeks after Hurricane Harvey. The salinity was ~15 at station 16 and decreasing when going further into East Bay (~10 at station 17 and 18; Fig. 7a). In upper GB, salinity at station 19-24 did not vary significantly (~15), increasing along with the distance away from the San Jacinto River mouth with highest value (~17.5) at

station 24. During both surveys, lowest Chl a (Fig. 7b) were observed adjacent to the nGOM, and the highest Chl a were closest to the river mouth. The photosynthetically Active Radiation (PAR) which were calculated from down-welling irradiance (not shown here) decreased significantly with depth, but surface PAR (Fig. 7c) were similar in magnitude at all stations. Pigment ratios including TChl a/TP (0.58-0.68), PSC/Chl a (0.07-0.26) and AP/TP (0.34-0.42) were obtained from HPLC measurements and shown in Figure 7d, 7e and 7f, respectively.

The CDOM calibrated and 0-0.5m depth averaged photosynthetic parameters F_V/F_M varied from 0.41 to 0.64 (Fig. 7g), while σ_{PSII} was in the range of 329-668 $Å^2 quantum^{-1}$(Fig. 7h). The highest σ_{PSII} and lowest F_V/F_M appeared adjacent to the nGOM (station 12-14). Conversely, values of F_V/F_M at stations 7-9 with a well-mixed water column were high with low values of σ_{PSII}. Both F_V/F_M and σ_{PSII} did not directly correlate with Chl a, (e.g., high Chl a ~51 µg L^{-1} at station 19 corresponded to a relatively low level of F_V/F_M ~0.45, versus high σ_{PSII} ~550 $Å^2 quantum^{-1}$). However, the stations with high F_V/F_M coincided with the high fraction of Chl a (Chl a/TP) and low fraction of AP (AP/TP) (Fig. 7d and 7f). In contrast, σ_{PSII} showed an overall positive relationship with AP/TP, but altered negatively with Chl a/TP during both surveys. The lowest (highest) value of σ_{PSII} (F_V/F_M) were observed at station 9 corresponding to the highest Chl a/TP value (~0.64) on October 29, 2017. The highest AP/TP and PSC/Chl a were obtained from stations adjacent to the nGOM.

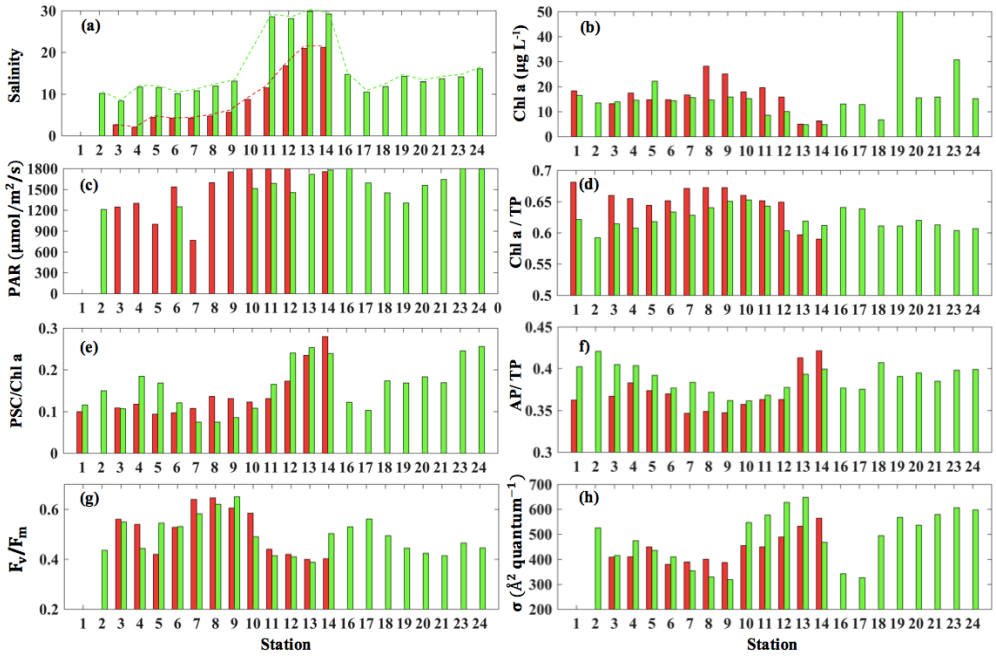

Figure 7. Environmental conditions (salinity, light field), pigment composition and physiological state in GB surface waters (red bars indicating samples from September 29, 2017 and blue bars representing samples from October 29 and 30, 2017). **(a)** Salinity, **(b)** Chl-a concentration, **(c)** PAR, **(d)** Chl a/TP, **(e)** PSC/Chl a, **(f)** AP/TP, **(g)** F_v/F_m, and **(h)** σ_{PSII}.

3.1.5 F_v/F_m and σ_{PSII} Taxonomic Signatures

Distinct pigments housed within phytoplankton light-harvesting antennae can strongly influence PSII light-harvesting capability and the photosynthetic quantum efficiency of phytoplankton (Lutz et al., 2001). In this study, we observed an inverse relationship (R^2 ~0.63-0.81; Fig. 8a and d) between the F_V/F_M and

σ_{PSII}, that appeared related to taxonomic signals during surveys 1 and 2 in GB. Stations 1-9 along the transect were considered as well-mixed group with no dominance by any particular group (black circles; Fig. 8a-c); stations 10-14 close to the entrance were however, strongly dominated by dinoflagellate and haptophyte (red symbol; Fig. 8a-c) during survey 1. This well-mixed group displayed low values of σ_{PSII} (~390-439 $Å^2 quantum^{-1}$), and high levels of F_V/F_M (~0.42-0.65) with F_V/F_M approaching 0.65 at station 9 on September 29, 2017 (Fig. 8a). However, enhanced contributions of dinoflagellate and haptophyte around the entrance corresponded to a decline of F_V/F_M (0.3~0.4) against an increase of σ_{PSII} (500~600 $Å^2 quantum^{-1}$) during survey 1. Furthermore, samples obtained from survey 2 at station 1-9, station 10-14, station 16-18 and station 19-24 were considered as well-mixed (black), dinoflagellate-haptophyte dominated (red), cyanobacteria dominated (blue) and cryptophyte-chlorophyte dominated (green), respectively. Stations 16-17 dominated by cyanobacteria (blue triangles; Fig. 8d) showed high level of F_V/F_M (0.5~0.6) and relatively low values of σ_{PSII} (300~400 $Å^2 quantum^{-1}$). The F_v/F_m and σ_{PSII} of cryptophyte-chlorophyte dominated stations showed a moderate level of F_V/F_M (0.4~0.5) and σ_{PSII} (580~680 $Å^2 quantum^{-1}$). More importantly, tight positive relationships existed between measurements of F_V/F_M and Chl a/TP (R^2~0.31-0.63; Fig. 8b and e). On the other hand, σ_{PSII} were positively correlated with PSC/Chl a with R^2~0.6 (Fig. 8c and f). The PSC/Chl a of cyanobacteria dominated group (blue symbols), and well mixed group (brown symbols) were relatively low. Highest PSC/Chl a and lowest Chl a/TP was observed for the dinoflagellate-haptophyte dominated group, corresponding to the lowest σ_{PSII} and highest F_V/F_M. In addition, cryptophyte-chlorophyte dominated group had high levels of PSC/TChl a (~0.18-0.26) and slightly higher Chl a/TP compared to dinoflagellate-haptophyte dominated group. Overall, well-mixed groups with high proportion of large-size phytoplankton (e.g., diatoms and chlorophyte) showed higher Chl a/TP along with larger F_V/F_M and smaller σ_{PSII} than those stations with high fraction of dinoflagellate and pico-populations (Fig. 8c and f).

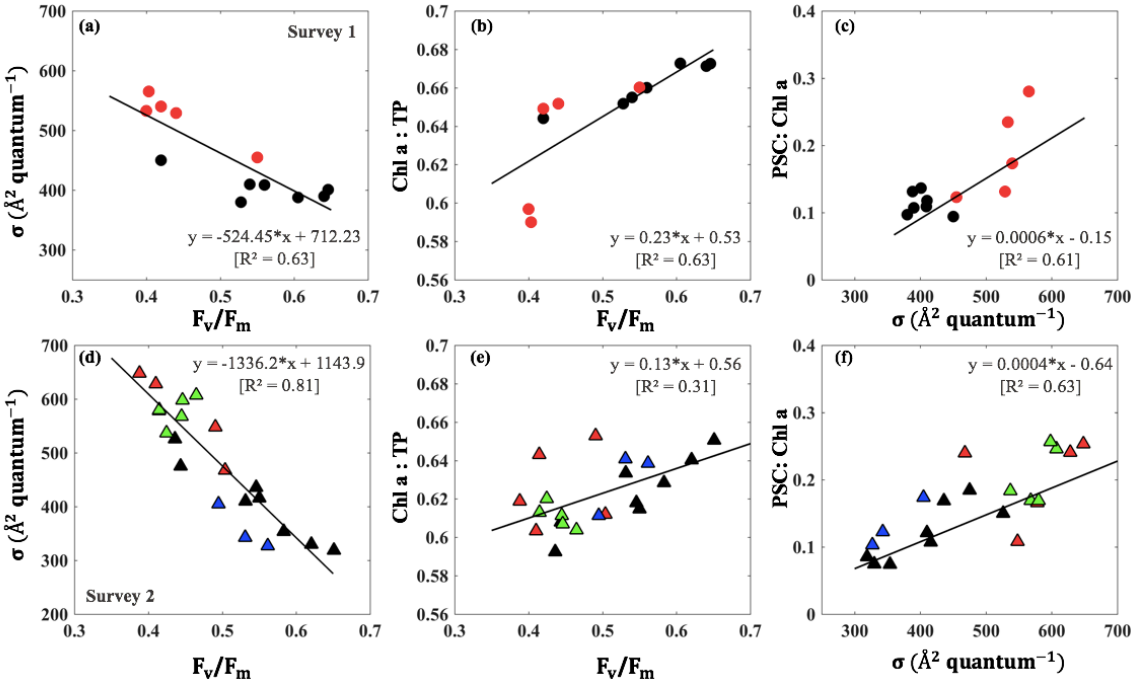

Figure 8. **a**, **d)** σ_{PSII} against F_V/F_M; **b**, **e)** F_V/F_M versus Chl a/TP; and **c**, **f)** σ_{PSII} versus PSC/Chl a on September 29 and October 29-30, 2017 respectively. The data points identified by dominant taxa with black, red, green and blue symbols denoting well-mixed, dinoflagellate-haptophyte dominated, cryptophyte-chlorophyte dominated, and cyanobacteria dominated groups, respectively.

3.2 Satellite Observations of Phytoplankton Pigments

3.2.1 An OLCI Chl a Algorithm and its Validation

Blue to green band ratio algorithms have been widely used to study Chl a in the open ocean and shelf waters (D'Sa et al., 2006; Blondeau-Patissier et al., 2014); however, these bands generally fail in estuarine waters due to strong blue absorption by the high levels of CDOM and suspended particulate matter, especially after flooding events associated with hurricanes (D'Sa et al., 2011; D'Sa et al., 2018; Joshi and D'Sa, 2018). The percentage contribution by CDOM fluorescence (blank) to maximum fluorescence yield (F_m) obtained from in-situ FIRe (Fig. 9a) demonstrated that Chl a fluorescence was strongly influenced by high amounts of CDOM fluorescence in GB, especially during the first survey (September 29, 2017), when the bay was under strong floodwater influence (red triangles; Fig. 9a). The CDOM fluorescence signal constituted ~ 25 % in the region adjacent to the nGOM (stations 12-14), between 25%-50% in the upper GB, and up to ~65% in Trinity Bay, which implied that blue and even green band are highly contaminated by CDOM and might not be the most suitable bands for estimating Chl a in GB. However, an increase in peak height near 700 nm and its shift towards longer wavelength (Fig. 3) can be used as a proxy to estimate Chl a concentration (Gitelson, 1992).

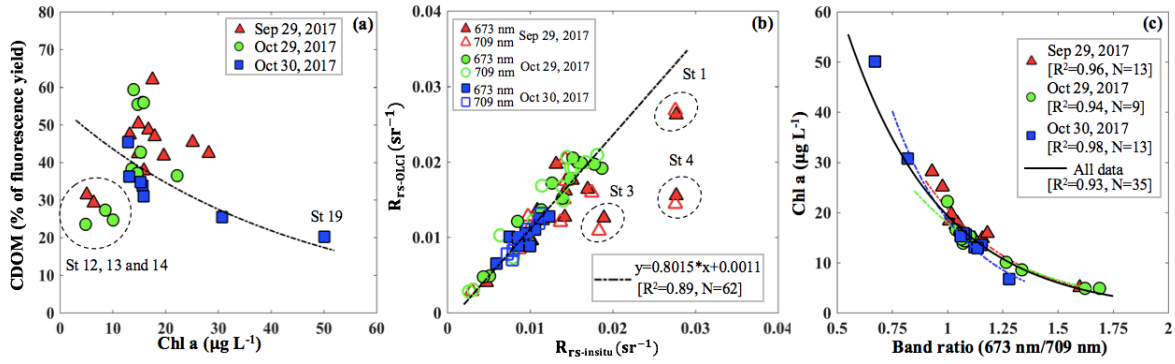

Figure 9. (a) Relationship between the percentage of the fluorescence yield of CDOM measured by FIRe against HPLC measured Chl a concentration. **(b)** Comparisons between R_{rs_insitu} and R_{rs_OLCI} at band 9 (673 nm) and band 11 (709 nm). **(c)** Exponential relationships between HPLC-measured Chl a concentrations and R_{rs_insitu} band ratio (673 nm/709 nm) in GB on September 29 (R^2=0.89), October 29 (R^2=0.93) and October 30 (R^2=0.97). Red, green and blue lines and symbols indicate data sets obtained on September 29, October 29 and 30, 2017 respectively.

The C2RCC atmospheric-corrected R_{rs_OLCI} at each of the sampling sites were further averaged (3×3 pixels) and compared with R_{rs_insitu} (Fig. 3) at phytoplankton red absorption (~673 nm) and Chl a fluorescence (~700 nm) bands (Fig. 9b). The C2RCC performed overall better for the second survey on October 29-30, 2017 (green and blue symbols; Fig. 9b) than the first survey on September 29, 2017 (red triangles; Fig. 9b) when stations 1, 3 and 4 (circled triangles; Fig. 3c) adjacent to the Trinity River mouth were included; these stations were the last sampling sites in the afternoon (~4:30 pm) and under somewhat cloudy conditions. The time difference between satellite pass and in-situ measurements, sky conditions and shallow water depth also likely introduced more errors at these locations. The R^2 between R_{rs_OLCI} and R_{rs_insitu} at red and near infrared (NIR) bands was 0.89 when the data from station 3 and 4 were excluded, suggesting good usability of these two bands for Chl a empirical algorithms in GB. Thus, the higher the Chl a concentration, the stronger the red light absorption, resulting in higher reflectance at 709 nm; consequently, negative correlations were observed between Red/NIR band ratio and Chl a. The ratio of Red (~673 nm) and NIR (709 nm) reflectance bands from in-situ measurements were overall highly correlated with HPLC-measured Chl a with R^2 ~ 0.96, 0.94 and 0.98 on September 29, October 29 and

October 30, 2017, respectively (Fig. 9c). The Sentinel-3A OLCI Chl a maps (Fig. 10a-c) were generated for all data based on the relationship between Chl a and the Red and NIR band ratio as:

$$\text{Chl a } (\mu g\ L^{-1}) = 216.38 \times \exp\left(-2.399 \times \frac{R_{rs}(673)}{R_{rs}(709)}\right) \quad \text{[All data]} \qquad \ldots\ldots (15)$$

The OLCI-derived Chl a (Fig. 10a-c) showed a good spatial agreement with Chl a$_{HPLC}$ (Fig. 10d-f). In addition, a comparison of this algorithm with that of Gilerson et al., 2010 revealed slightly better performance (not shown) inside of GB and especially in the area adjacent to the shelf.

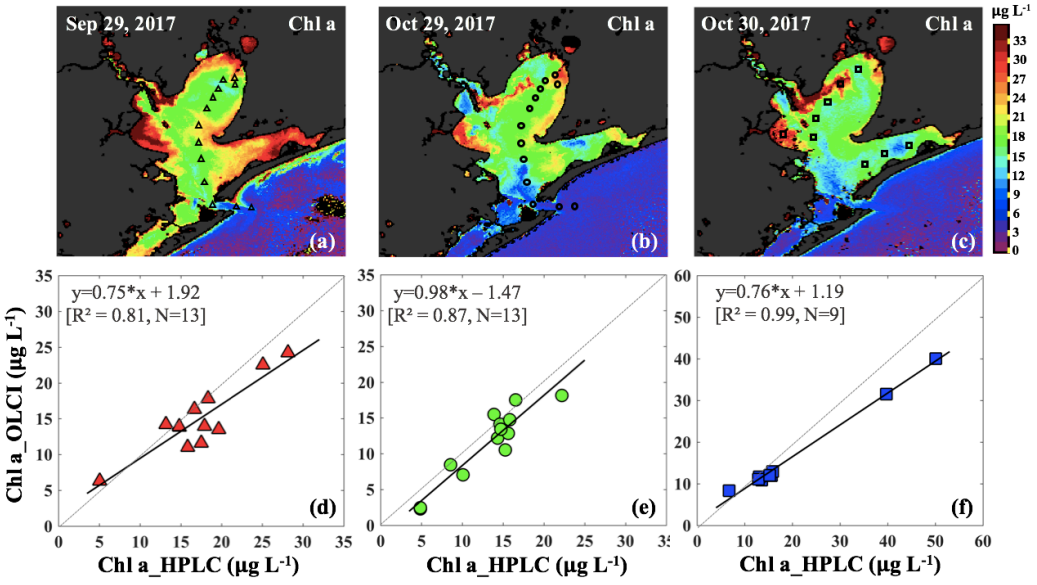

Figure 10. Chl a concentration generated based on in-situ band ratio ($R_{rs}673/R_{rs}709$) algorithm with (a), (b) and (c) representing Chl a distribution on September 29, October 29 and October 30, 2017, respectively; (c), (d) and (f) show the validation between HPLC-measured Chl a and OLCI-derived Chl a on September 29, October 29 and October 30, 2017, respectively.

The Chl a concentration on September 29, 2017 was overall higher than that on October 29-30, 2017 through the entire bay. East Bay displayed very high Chl a concentration, with highest value (>30 μg L^{-1}) observed on September 29, 2017 (Fig. 10a). The narrow shape and shallow topography of East Bay results in relatively higher water residence time (Rayson et al. 2016); thus, the reduced exchange with shelf waters likely lends the East Bay vulnerable to eutrophication. The average Chl a concentration on October 29-30, 2017 were ~ 15 μg L^{-1} along the transect (station 1-11) and ~4-6 μg/L (station 12-14) close the entrance of GB. In addition, Chl a adjacent to San Jacinto River mouth (>16 μg L^{-1}) was higher than that in Trinity Bay, which might suggest that San Jacinto inflow had higher nutrient concentrations than Trinity as also previously reported (Quigg et al., 2010). Furthermore, the OLCI-Chl a maps on October 29 and 30, 2017 showed extremely high Chl a concentration in a narrow area adjacent to the San Jacinto River mouth, with Chl a approaching ~ 40 μg L^{-1} at station 19 (Fig. 10c).

3.2.2 Long-term Chl a Observations in Comparison with Hurricane Harvey Event

OLCI-derived Chl a maps between August, 2016-November, 2017 (Fig. 11a_1-a_{15}) and time series of averaged Chl a values in the areas of Trinity Bay, East Bay and adjacent to the nGOM (Fig 11b) revealed regionally different responses of Chl a to freshwater discharge from the San Jacinto and the Trinity Rivers (Fig. 11b). Due to the relatively much higher discharge from the Trinity River, the spatial distribution of Chl a in the bay (Fig. 11) generally indicates its greater influence than the San Jacinto River. During the

winter, and spring in 2017, phytoplankton Chl a peaks ~32 μgL^{-1} in Trinity Bay (Fig. 11b) were observed after high inflows from both rivers (Fig. $11a_5$-a_8). Chla then slightly decreased to ~20 μgL^{-1} in summer (July and August, 2017). Generally, Chl a showed overall lower value (~10 μgL^{-1}) between September-December, 2016 compared to 2017 in the absence of meteorological and hydrological events (Fig. $11a_1$-a_4). However, with the East Bay less directly affected by river discharge, Chl a levels remained fairly constant in the range of ~18-24 μgL^{-1} before hurricane. In contrast, extremely high river discharge (~3300 m^3s^{-1}) induced by Hurricane Harvey in late August, 2017, elevated Chla in both Trinity and East Bay to higher levels as observed on September 14, 2017 (~30-35 μgL^{-1}; Fig. $11a_{11}$) compared to mean state of fall season in 2016. Chl a then continuously decreased through September to October, 2017 in Trinity and East Bay and were relatively low ($\leq$10 μgL^{-1}) in November, 2017 under no additional pulses of river discharge. Concentration of Chla adjacent to the entrance of GB exhibiting much lower values year round than that of the Trinity and East Bay, and also showed slight positive responses to the enhanced river discharge and the hurricane-induced flooding events. In addition, Chl a concentrations always displayed low values along the Houston Ship Channel.

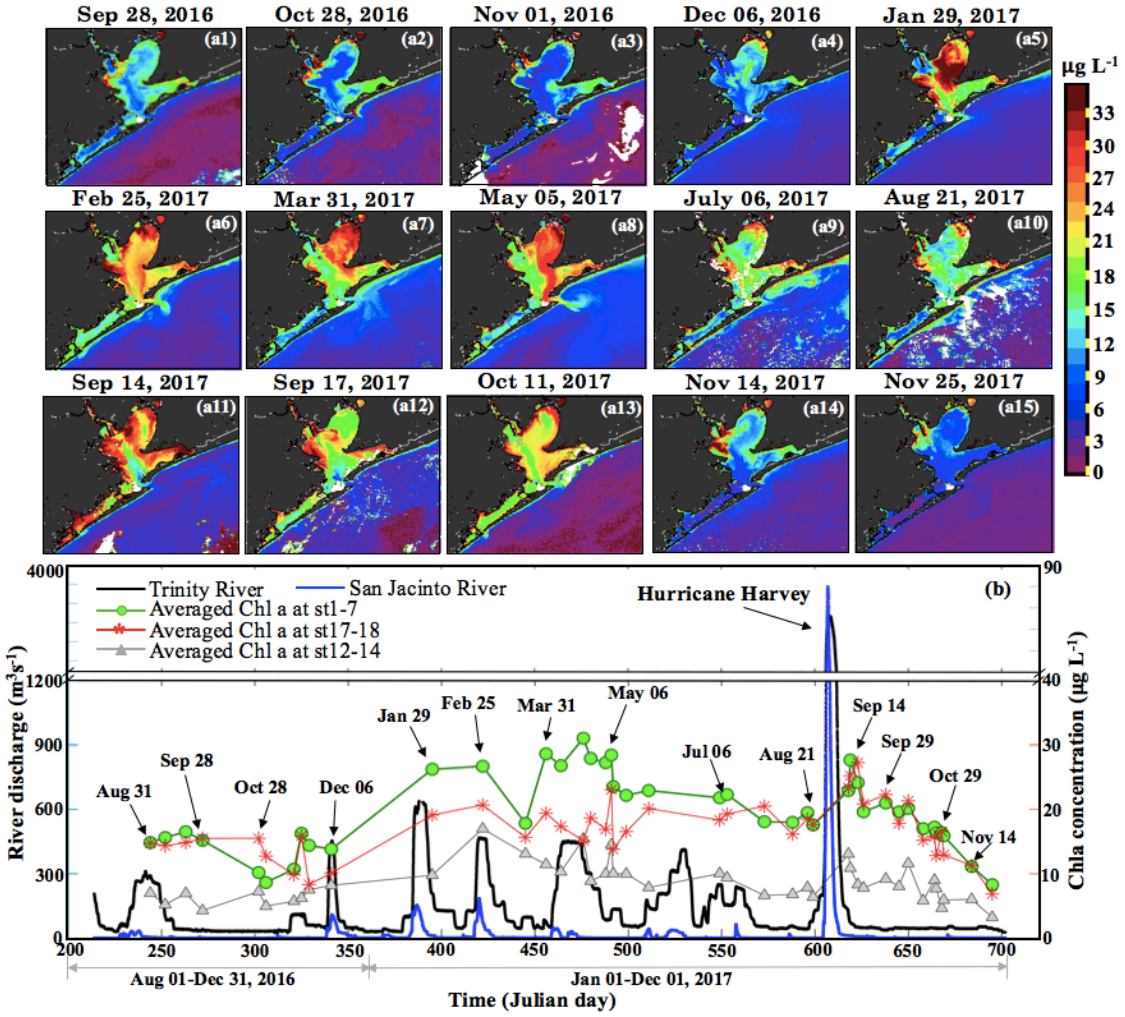

Figure 11. **(a_{1-15})** OLCI-derived Chl a shown for the period of August 31, 2016-November 25, 2017. **(b)** Trinity River discharge at Romayor, Texas (USGS 08066500, black line) and the west flank of the San Jacinto River (USGS 08067650; blue line); the green, red and gray lines/symbols represent the mean of Chl a at stations 1-7 in Trinity Bay, at stations 17-18 in East Bay and at stations 12-14 close to the

entrance of GB corresponding to 43 cloud free Sentinel 3A-OLCI images (colored symbols; dated symbols correspond to images $\mathbf{a_{1\text{-}15}}$).

3.2.3 Reconstruction of Total Pigment Absorption Spectra from OLCI-derived Chl a

The reconstructed $a_{pig}(\lambda)$ based on the third order function of Chl a_HPLC (gray lines; Fig. 12a and b) agreed well with the spectrophotometrically measured $a_{pig}(\lambda)$ (black lines; Fig. 12a and b) during both surveys (R^2=0.86; Fig. 12c). The R^2 for modeled versus measured $a_{pig}(\lambda)$ are between 0.76 and 1.00 from 400 to 700 nm with averaged R^2 of whole spectra reaching ~ 0.82 on September 29, 2017 and ~0.89 on October 29-30, 2017, respectively. The vector coefficients $C = [C_3, C_2, C_1, C_0]$ obtained from Eq. (11) were further applied to Eq. (12) to generate $a_{pig\_OLCI}(\lambda)$ based on OLCI-derived Chl a images on July 06 (Fig. 11a_9), September 29 (Fig. 10a), October 29-30 (Fig. 10b-c), and Nov 25 (Fig. 11a_{15}), 2017, respectively; these contained 259×224 pixels in each image. The $a_{pig\_OLCI}(\lambda)$ at each pixel was retrieved at 1 nm interval, and thus 301 images of $a_{pig\_OLCI}(\lambda)$ representing each wavelength were obtained over GB.

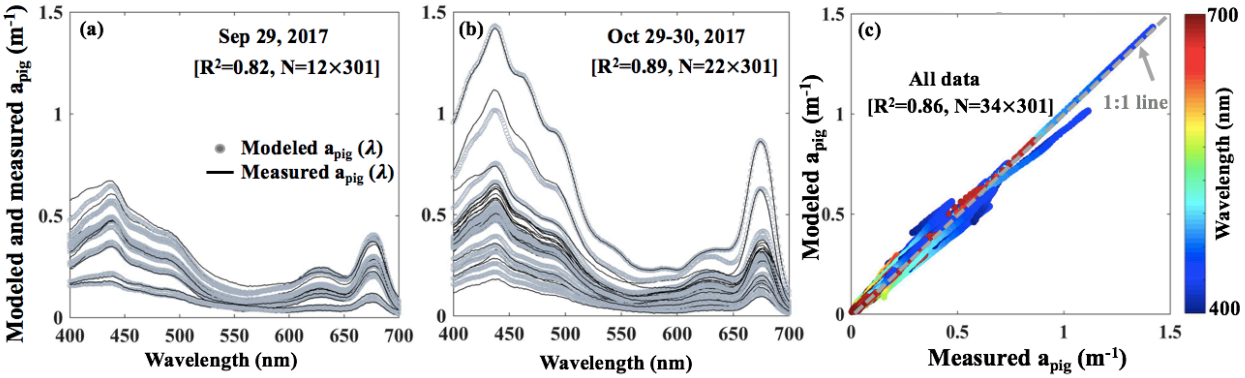

Figure 12. Spectrophotometrically measured and multi-regression fitted $a_{pig}(\lambda)$ spectra acquired on **(a)** September 29 and **(b)** October 29-30, 2017 in GB. Gray and black lines represent modeled and measured results, respectively. **(c)** Comparison between modeled and spectrophotometrically measured $a_{pig}(\lambda)$ for all data with color representing wavelength.

3.2.4 Accuracy of phytoplankton pigment retrievals from Sentinel 3A-OLCI

The reconstructed $a_{pig\_OLCI}(\lambda)$ was spectrally decomposed into 16 individual pigment spectra at each pixel based on Eq. (14). A comparison of HPLC-measured pigments to averaged NNLS inversion model retrieved pigments showed that R^2 ranged from a low of 0.39 for violaxanthin to 0.98 for Chl a and mean error was in the range of 11.36%-60.98% (Table 4). The NNLS-modeled Chl a also correlated well with OLCI-derived Chl a (R^2=0.98; Fig. 13a), with each exhibiting similar quantitative and spatial patterns. For the other 15 simultaneously simulated pigments, only 7 pigments averaged R^2 value greater than 0.65 (Table 4). Five NNLS-derived versus HPLC measured diagnostic pigments including alloxanthin, Chl b, zeaxanthin, fucoxanthin and peridinin are shown in Figure 13. The R^2 between NNLS-derived and HPLC-measured pigments for surveys 1 and 2 was highest for alloxanthin (0.91; Fig. 13b). For the other pigments R^2 was 0.78 for Chl b (Fig. 13c), 0.69 for zeaxanthin (Fig. 13d), 0.51 for fucoxanthin (Fig. 13e) and 0.50 for peridinin (Fig. 13f), respectively.

Table 4. Correlation between HPLC-measured pigment concentration with NNLS-modeled pigments.

Pigments	Sep 29, 2017 (R^2)	Oct 29, 2017 (R^2)	Oct 30, 2017 (R^2)	Averaged (R^2)	Mean error (%)
Chl a	0.95	0.97	0.98	0.97	11.36
Chl b	0.76	0.77	0.95	0.82	24.58
Chl c_1	0.56	0.42	0.79	0.59	34.23
Chl c_2	0.49	0.45	0.74	0.56	31.13
Pheophythin a	0.76	0.79	0.72	0.75	17.77
Pheophythin b	0.75	0.88	0.76	0.79	15.65
Peridinin	0.65	0.48	0.51	0.54	42.26
Fucoxanthin	0.65	0.45	0.85	0.60	30.51
Neoxanthin	0.55	0.63	0.79	0.65	31.13
Lutein	0.61	0.78	0.72	0.70	32.54
Violaxanthin	0.43	0.34	0.39	0.39	60.98
Alloxanthin	0.81	0.40	0.91	0.72	32.90
Diadinoxanthin	0.69	0.40	0.89	0.66	48.12
Diatoxanthin	0.49	0.43	0.49	0.47	54.23
Zeaxanthin	0.76	0.65	0.78	0.73	19.03
β-carotenoid	0.41	0.42	0.82	0.55	44.02

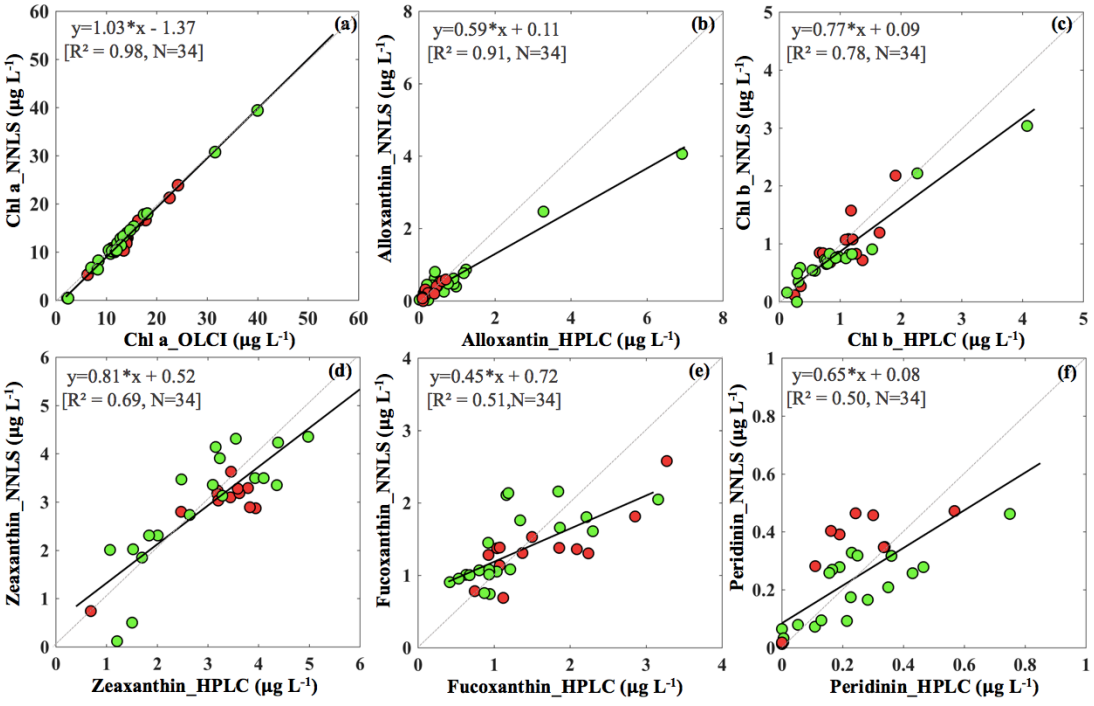

586

587 **Figure 13**. Sentinel-3A OLCI derived pigment concentration against HPLC measured pigment
588 concentration in Galveston Bay; **a)** Chl a, **b)** alloxanthin, **c)** Chl-b, **d)** zeaxanthin, **e)** fucoxanthin, and **f)**
589 peridinin.

590 ### 3.3.1 Spatiotemporal Variations of Diagnostic Pigments

591 Flooding due to Hurricane Harvey not only enhanced Chl a, but also affect the phytoplankton pigments
592 composition. NNLS-retrieved pigment maps in July, September, October, and November, 2017 including
593 those of alloxanthin, chl b, zeaxanthin, fucoxanthin and peridinin (Fig. 14) showed different levels of
594 variations before and after the hurricane event. Alloxanthin, which is unique to cryptophytes (Wright and
595 Jeffrey, 2006) exhibited same spatial distribution patterns (Fig. 14a_1-e_1) with Chl a. Alloxanthin was

596 especially low (~ 0.5 μg L^{-1}, Fig. 14a_1) in the major basin area on July 06, 2017 before the hurricane and
597 slightly elevated (~0.7 μg L^{-1}, Fig. 14b_1) in September and October, 2017 after the hurricane passage.
598 Furthermore, extremely high alloxanthin (~ 3.5 μg L^{-1}, Fig. 14c_1-d_1) was observed adjacent to San Jacinto
599 River mouth on October 29-30, 2017, which coincided with the high %Chl a of cryptophyte at stations 19
600 and 23 (Fig. 6b). The bloom with high concentration of alloxanthin on October 29, 2017 (~3.5 μg L^{-1}; Fig.
601 14c_1) then extended to a broader area on October 30, 2017 (Fig. 14d_1).
602
603 Chl b is abundant in the group of chlorophyte (green algae) (Hirata et al., 2011) and the spatial
604 distributions of Chl b (Fig. 14a_2-e_2) also showed strong correlations with Chl a on July 06, 2017,
605 September 29, October 29-30 and November 25, 2017. The NNLS-derived Chl b exhibited overall low
606 values (~0.5-2 μg L^{-1}; Fig. 14a_2) before the hurricane and showed obvious elevation throughout bay after
607 the hurricane and eventually decreasing to pre-hurricane level by November 25, 2017. Furthermore, Chl b
608 concentrations observed on September 29, 2017 were higher than that on October 29-30, 2017, which
609 corresponded to a decline of chlorophyte percentage derived from the IOP inversion algorithm (Fig. 6).
610 More importantly, images obtained from IFCB at the entrance to GB also detected freshwater species
611 Chlorophyte (*Pediastrum duplex;* Fig. 14g) on September 29, 2017. However, this species was rarely
612 observed in IFCB images for the other dates (Fig. 14a_1 and Fig. 14c_1-e_2). In addition, Chl b concentrations
613 approached ~2.8 μg L^{-1} in the bloom area and the corresponding green discoloration of water was also
614 observed during the field survey on October 30, 2017.

615 Zeaxanthin is known as taxa-specific pigment for prokaryotes (cyanobacteria) (Moisan et al., 2017;
616 Dorado et al., 2015) and NNLS-derived zeaxanthin maps (Fig. 14a_3-e_3) displayed significantly different
617 patterns with Chl a, exhibiting low concentrations in the areas where the Chl a were high. For example,
618 zeaxanthin was especially low in the bloom area on October 29-30, 2017, which agreed well with
619 low %Chl a of cyanobacteria at stations 19 and 23 (Fig. 6), thus indicating that this localized algal bloom
620 event was not associated with cyanobacteria. In addition, zeaxanthin was high ~ 3.0 μg L^{-1} (Fig. 14a_3) in
621 both GB and shelf waters on July 06, 2017 before the hurricane event. Later, zeaxanthin increased a
622 slightly on September 29, 2017 (Fig. 14b_3) with IFCB data detecting N_2-fixing cyanobacteria (*Anabaena*
623 spp.; Fig. 14g) and remained elevated on October 29-30, 2017 (Fig. 14b_3-c_3). Zeaxanthin eventually
624 decreased to very low values (~ 1.2 μg L^{-1}; Fig. 14e_3) on November 25, 2017.

625 Fucoxanthin is a major carotenoid found in diatoms (Hirata et al., 2011; Moisan et al. 2017) and the
626 NNLS-derived fucoxanthin maps (Fig. 14a_4-e_4) showed highly similar distribution patterns with Chl a.
627 Maps of fucoxanthin showed low concentrations on July 06, 2017 (~1.5 μg L^{-1}; Fig. 11a_4), and displayed
628 a large increase on September 29, 2017 (~1.6-3.0 μg L^{-1}; Fig. 11b_4). Diatom group detected from IFCB
629 were dominated by marine species before the hurricane, but subsequently shifted to freshwater species
630 (e.g., *Pleurosigma*; Fig. 14g) and then back to marine species after October, 2017. Overall, fucoxanthin
631 concentrations in GB were relatively higher during survey 1, which corresponded to the higher %Chl a of
632 diatom (Fig. 6) compared to survey 2. Fucoxanthin continuously decreased to low values on November
633 25, 2017 (~1.6 μg L^{-1}; Fig. 11e_4), but accounted for higher fraction of phytoplankton diagnostic pigments
634 compared to other dates in July, September and October, 2017.
635
636 Peridinin, a primary bio-marker pigment for certain dinoflagellates (Örnólfsdóttir et al., 2003), also
637 displayed significantly distinct patterns in comparison to Chla (Fig. 14a_5-e_5). On July 06, 2017, peridinin
638 was ~0.24-0.36 μg L^{-1}, accounting for high proportion of the diagnostic pigments; meanwhile, diversity of
639 marine dinoflagellate species observed from IFCB at this time was as also high (Fig. 14f). However,
640 peridinin decreased (~0.001-0.05 μg L^{-1}) after the hurricane, with freshwater dinoflagellate species
641 (*Ceratium hirundinella*; Fig. 14g) detected from IFCB on September 29, 2017. In addition, maps of
642 peridinin during both surveys (Fig. 14b_5-d_5) presented higher concentration (~0.3 μg L^{-1}) in higher salinity
643 waters adjacent to the bay entrance, which agreed well with the increasing fraction of dinoflagellate at

station 10-14 detected from IOP inversion model (Fig. 6). In contrast, peridinin showed low concentrations in both GB and shelf waters (Fig. 14e$_5$), with dinoflagellate species rarely observed from IFCB on November 25, 2017 (Fig. 14*l*).

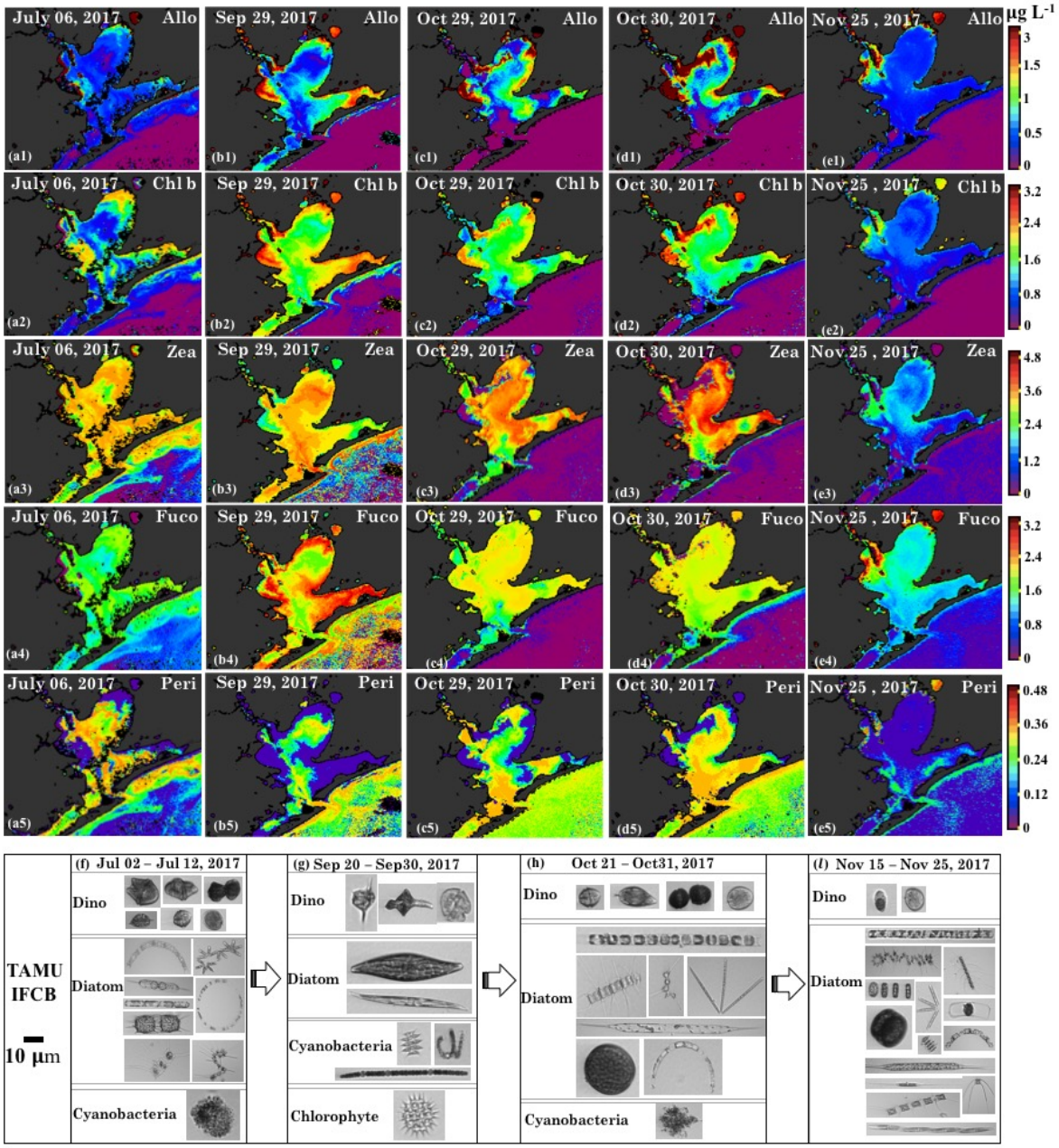

Figure 14. Sentinel-3 OLCI derived maps of diagnostic pigments for Galveston Bay. Simulated **a1-e1)** alloxanthin, **a2-e2)** Chl b, **a3-e3)** zeaxanthin, **a4-e4)** fucoxanthin, and **a5-e5)** peridinin concentrations. a, b, c, d and e represent columns (maps for July 06, September 29, October 29-30 and November 25, 2017) and 1-5 represent rows (pigments), respectively; **(f)**, **(g)**, **(h)** and **(*l*)** are the corresponding IFCB data for July 06, September 29, October 29-30 and November 25, 2017, respectively; note that IFCB pictures of fresh water species including chlorophyte and cyanobacteria that appeared on September 20-30, 2017 have been zoomed in for better clarity.

4 Discussion

4.1 Performance of the Semi-Analytical IOP Inversion Algorithm

The residuals between R_{rs_insitu} and R_{rs_mod} on September 29 and October 29-30, 2017, are negative in the blue (400-450 nm) and red (610-630 nm) spectral range at most stations, whilst keeping positive ~700 nm, which could be attributed to a number of factors. First, the underestimation near 700 nm by the IOP inversion model is possibly induced by the absence of a fluorescence component in the IOP inversion model; thus, R_{rs_insitu} containing fluorescence signals were generally higher than R_{rs_mod} near 700 nm. Second, in the range of 610-630 nm, the absorption was overestimated at most of the stations; in this spectral range, the shape of spectra was strongly modulated by cyanobacteria absorption. Thus this overestimation ~620 nm is likely introduced by the input absorption spectrum (eigenvector) for cyanobacteria since all of input $a^*_{phi}(\lambda)$ are general absorption spectral shapes for different phytoplankton groups. However, the spectra of $a^*_{phi}(\lambda)$ can vary in magnitude and shape associated with package effects under different environmental conditions (e.g. nutrient, light and temperature) even for the same species (Bricaud et al., 2004). More detailed absorption spectra of phytoplankton under different conditions (e.g. high/low light and nutrient) could improve the performance of the IOP algorithm. Furthermore, the role of scattering might be another key factor to explain differences between R_{rs_insitu} and R_{rs_mod} for the whole spectra. The quantity and composition of suspended materials including phytoplankton, sediment and minerals will collaboratively determine $b_{bp}(\lambda)$ in both shape and magnitude. However, the input eigenvector of $b_{bp}(\lambda)$ in the present study was not divided into detailed sub-constituents and was a sum spectrum based on a power law function (Table 2). In reality, $b_{bp}(\lambda)$ spectra are not smooth and regular, and thus, the $b_{bp}(\lambda)$ value of phytoplankton and sediment might introduce errors to the whole spectrum due to their own scattering characteristics.

4.2 Distributions of NNLS-Retrieved Phytoplankton Pigments from Sentinel-3A OLCI

The derived maps of phytoplankton diagnostic pigments appeared to be reasonably correlated with HPLC-measured diagnostic pigments and showed overall agreement with extracted phytoplankton taxonomic compositions detected from the IOP inversion algorithm. The retrieved diatom-specific fucoxanthin maps however, showed high concentrations compared to other pigments adjacent to the entrance (Fig. 13b_4 and c_4), which contradicted with diatom %Chl a calculated from IOP inversion algorithm that Chl a fraction of diatom was relatively uniform at stations 12-14 (Fig. 6b). (Nair et al., 2008) concluded that fucoxanthin can occur in other phytoplankton types (e.g. raphidophyte and haptophyte). Fucoxanthin and/or fucoxanthin derivatives such as 19′-hexanoyloxyfucoxanthin can also replace peridinin as the major carotenoid in some dinoflagellates (e.g., *Karenia brevis*; Jeffrey and Vest, 1997). The elevated contributions from groups of dinoflagellate, haptophyte and prochlorophyte adjacent to the entrance (stations 10-14; Fig. 6b) along with high concentrations of fucoxanthin likely suggest the presence of elevated fractions of haptophyte and dinoflagellate, and further implies that fucoxanthin is an ambiguous marker pigment for diatoms. This could also explain the poor correlation between inverted %Chl a and %DP observed for the groups of diatom and haptophyte (Fig. 4g and l). These results also further suggest the inherent limitations of using DP-type comparison between major biomarker pigments and phytoplankton groups because the major assumption for DP-type methods is that diagnostic pigment of distinct phytoplankton groups are uncorrelated to each other. This assumption is invalid in that concentrations of major biomarker pigments are significantly correlated with each other and also may vary in time and space under some external environmental stress (e.g., temperature, salinity, mixing, light and nutrient) (Latasa and Bidigare, 1998).

Chl a concentration is another crucial factor that influences the accuracy of retrieved pigments. The goal of the empirical Chl a algorithm for Sentinel 3A-OLCI is to obtain more accurate estimation of surface

Chl a concentration, which is better for retrieving other accessory pigments. However, the primary limitation of Chl a empirical algorithms in this study was that the derived relationships between Red/NIR and Chl a in GB may only be valid within a specific time period due to temporally-limited field observations versus highly dynamic estuarine environments. Therefore, a Chl a empirical algorithm that is more broadly applicable over a longer time period will largely improve the accuracy of retrieved pigments over a series of remote sensing images and can be more useful for spatiotemporal studies of phytoplankton functional diversity. In addition, the similarity of many carotenoid absorption spectra could as well introduce errors when applying spectral decomposition techniques. Thus, the 16 input pigment spectra used in this study were selected from Thrane et al., 2015, which were correctly identified from unknown phytoplankton community structure with low error rate reported from Monte Carlo tests to minimize the potential effects of aliasing the spectra.

4.3 Response of Phytoplankton Taxa to Environmental Conditions

Previous studies showed diatoms to be the most abundant taxa in GB, and tend to be more dominant during winter/spring, corresponding to periods of high fresh water discharge and nutrient-replete conditions (Dorado et al., 2015; Örnólfsdóttir et al., 2004a); transition from chain-forming diatoms such as *Chaetoceros* and rod-like diatoms pre-flood to small cells, such as *Thalassiosira* and small pennate diatoms were generally observed during high river discharge periods (Lee, 2017). In contrast, cyanobacteria were the most abundant species during the warmer months (Jun-Aug) when river discharge was relatively low (Örnólfsdóttir et al., 2004b). Further, phytoplankton groups in GB responded differentially both taxonomically and spatially to the freshening events due to their contrasting nutrient requirements and specific growth characteristics. For instance, most phytoplankton taxa (e.g., diatom, chlorophyte and cryptophyte) can be positively stimulated by fresh inflows due to their relatively rapid growth rate (Paerl et al., 2003); however, Roelke et al. (2013) also documented that cyanobacteria and haptophytes in the upper GB were not sensitive to nutrient-rich waters from both rivers, due to the extra nutrients obtained from N_2-fixation abilities and mixotrophic characteristics, respectively. In the lower part of GB, dinoflagellates and cyanobacteria are known to be more dominant during the low river discharge due to their preference for higher phosphorus (P) compared to some other groups, and to low turbulence (Lee, 2017) and thus, generally inversely related to the fresh inflows (Lee, 2017; Roelke et al., 2013).

Perturbations following Hurricane Harvey affected the phytoplankton taxonomic composition with alterations in phytoplankton community structure observed as the GB system transitioned from marine to freshwater then to marine system (Figs. 6 and 14). Higher fraction of zeaxanthin and peridinin and the presence of large and slow-growing marine dinoflagellates detected from IFCB pre-hurricane (July 06, 2017) indicate that both cyanobacteria and dinoflagellates were the main groups of phytoplankton community during summer, and likely associated with warmer temperature and lower river flow (Lee, 2017). Later, massive Chla observed in September, 2017 and the decline of Chla to background state in October, 2017, were likely associated with the hurricane-induced high river discharge and the resulting variations in nutrient concentration and composition. Higher fractions of diatom and chlorophyte accompanied with increasing fucoxanthin and Chl b on September 29, 2017, to some extent agreed well with measurements of Steichen et al., 2018 two weeks following Hurricane Harvey that freshwater species (diatom, green algae and cyanobacteria) appeared immediately following the flooding event. Greater abundance of diatom and chlorophyte during survey 1 in comparison to survey 2 were likely due to their rapid growth rates, enhanced nutrient uptake rates, and tolerance of low salinity and high turbulence under high nutrient loading conditions following the freshwater inflows (Roy et al., 2013; Santschi, 1995). Therefore, it is not surprising that Chl b concentrations showed very low values in July and November, 2017, when river discharge was correspondingly low. Cyanobacteria, which normally prefer low salinity conditions, also showed specific responses to this flood event. On September 29, 2017,

zeaxanthin slightly increased compared to summer season in July, 2017. The decline of diatoms and chlorophyte versus slightly increased cyanobacteria observed on October 29-30, 2017, could be attributed to the relatively slow growth rates of cyanobacteria compared to that of chlorophytes and diatom (Paerl et al., 2003); cyanobacteria appeared to have lagged behind these groups in terms of responding to enhanced freshwater discharge when longer residence times were again restored. In contrast, the presence of green algae and cyanobacteria could as well as be explained by the clarity and turbidity gradient of water. Quigg et al. (2010) reported that when turbidity was relatively high, chlorophyte dominated over cyanobacteria with biomass ratio of chlorophyte/cyanobacteria greater than 2, which supported our observations that chlorophyte dropped off whilst cyanobacteria increased during survey 2 on October 29-30, 2017. In addition, highest cyanobacteria percentage in East Bay suggest that calm and stratified waters may accelerate cyanobacteria growth as the buoyancy regulation mechanism of cyanobacteria is possibly restricted by the water mixing (Roy et al., 2013). Peridinin, which initially decreased in September and then increased in the lower GB on October 29-30, 2017, suggest that dinoflagellates showed overall preference for high-salinity waters. Furthermore, previous IFCB observations from Biological and Chemical Oceanography Data Management Office (BCO-DMO) showed that algal blooms after hurricanes in the nGOM were initially dominated by diatoms, and subsequently transitioned to blooms of dinoflagellates, likely associated with nutrient ratios and chemical forms of nutrient supplied by the flood waters and rainfall (Heisler et al., 2008). In addition, high concentrations of peridinin observed along the Houston Ship Channel, might provide evidence that the ballast water addition from shipping vessels likely promote harmful species of dinoflagellates (Steichen et al., 2015). Finally, low concentrations of all pigments on November 25, 2017 with relatively higher fraction of fucoxanthin compared to previous dates (Fig. 14), indicate the major role of marine diatoms at that time and further confirms that diatoms can be found under a wide range of inflows in GB.

The localized cryptophyte-chlorophyte bloom that occurred ~60d after Hurricane Harvey on October 29-30, 2017, was captured by both satellite and in-situ measurements. This bloom might not be associated with the flooding events of Hurricane Harvey, and could be linked to nutrient-rich runoff flowing into GB, reflecting sensitivity and rapid response of phytoplankton community to nutrient input in GB. In shallow and turbid estuaries, human activities are altering the environment and causing phytoplankton changes in diversity and biomass to occur more frequently. Dugdale et al. (2012) reported that variations of phytoplankton community in San Francisco estuary could be attributed to anthropogenically-elevated concentration of ammonium, which restrain the uptake of nitrate, thus reducing the growth and reproduction of larger diatoms and shifting towards smaller species (e.g., cryptophyte and green flagellate). Furthermore, 'pink oyster' events related to alloxanthin of cryptophyte in GB occurred more frequently from September through October in recent years (Paerl et al., 2003). The eastern side of Houston Channel in mid bay region was reported as the area most heavily impacted by the intense 'pink oyster' events. Previous studies and present observations both suggest that this cryptophyte-chlorophyte dominated bloom could be promoted by the nutrient-driven eutrophication from Houston Ship Channel, urbanization and industrialization along the upper San Jacinto River complex.

4.4 Photo-Physiological State of Natural Phytoplankton Community

In this study, the CDOM-corrected F_V/F_M and σ_{PSII} likely represented a composite of both phytoplankton taxonomy and physiological stress (e.g., nutrient and mixing). Typically, lowest N and P concentrations were measured closest to the nGOM (Quigg et al., 2009). Phytoplankton community living close to nGOM were usually in poor nutrient conditions and would be expected to maximize their light harvesting (increase in σ_{PSII}) due to nutrient stress. Simultaneously, phytoplankton cells might experience a decline of functional proportion of reaction centers of PSII (RCII), which means decrease in F_V/F_M. The observed low levels of F_V/F_M and Chl a/TP versus high values of σ_{PSII} and AP/TP adjacent to the nGOM showed agreement with previous studies that the fraction of carotenoids to be higher for nutrient-poor cultures

(Schitüter et al., 1997; Holmboe et al., 1999). In contrast, phytoplankton in well-mixed waters (station 7-9) might experience abundant nutrients due to the resuspension of cyclonic gyre around Smith Points; as such, their photosynthetic machinery were likely healthier. Aiken et al. (2004) documented that the Chl a/TP ratio was relatively higher when plants were in good growing conditions, which is similar to the observations in this study that phytoplankton have higher fraction of Chl a accompanying higher rate of photosynthetic efficiency (F_V/F_M) under nutrient replete conditions. Overall, the spatial pattern of F_V/F_M and σ_{PSII} in GB could be mainly attributed to physiological stress of nutrient and hydrodynamics conditions since the light availability (PAR) during the sampling period did not spatially vary significantly at the surface. Furthermore, FIRe measurements (F_V/F_M and σ_{PSII}) also presented a taxonomic signal super-imposed upon environmental factors. Each cluster with different dominant taxa (well mixed group, chlorophyte & cryptophyte, cyanobacteria, and dinoflagellate & haptophyte) displayed different physiological characteristics. The taxonomic sequence of eukaryotic groups from high F_V/F_M, low σ_{PSII} to low F_V/F_M, high σ_{PSII} in the present observations showed potential effects of phytoplankton cell size corresponding to diatoms, chlorophyte, and cryptophyte, dinoflagellate and haptophyte. The prokaryote (cyanobacteria) had relatively high values of F_v/F_m and low values of σ_{PSII}; this agreed with F_V/F_M for some species of nitrogen-fixing cyanobacteria that can range from 0.6 to 0.65 (Berman-Frank et al., 2007). Yet, it is difficult to separate the contributions from environmental factors and taxonomic variations to the changes of FIRe fluorescence signals since all these parameters are inter-related. Different phytoplankton groups/sizes will display distinct physiological traits (F_V/F_M and σ_{PSII}) when experiencing considerable environmental pressures. Thus, effects of physiological stress on F_V/F_M and σ_{PSII} variations for natural samples can only be determined when taxonomic composition can be excluded as a contributor (Suggett et al., 2009).

5 Conclusions

Field measurements (salinity, pigments, optical properties and physiological parameters) and ocean color observations from Sentinel-3A OLCI were used to study the effects of extreme flooding associated with Hurricane Harvey on the phytoplankton community structures, pigment distributions and their physiological state in GB. Flooding effects made the entire GB transition from saline to freshwater then back to a more marine influenced system. The band ratio (Red/NIR) of R_{rs_insitu} were negatively correlated with HPLC-measured Chl a in an exponential relationship ($R^2 > 0.93$). The satellite-retrieved Chl a maps yielded much higher Chl a concentration on September 29, 2017 compared to October 29-30, 2017 with lowest Chl a observed adjacent to the shelf waters. Phytoplankton taxonomic composition was further retrieved from R_{rs_insitu} using a 10-species IOP inversion algorithm. Phytoplankton community generally dominated by estuarine marine diatoms/dinoflagellates before flood events, was altered to freshwater species of diatom, green algae (chlorophyte) and cyanobacteria during survey 1. It also showed an increase of small-size species including cryptophyte, haptophyte, prochlorophyte and cyanobacteria accompanied by a decline of chlorophyte and diatoms during survey 2.

Phytoplankton diagnostic pigments were retrieved using an NNLS inversion model based on Sentinel-3A OLCI Chl a maps also confirmed spatiotemporal variations of phytoplankton taxonomy. The NNLS-retrieved diagnostic pigment maps showed overall spatiotemporal agreement with HPLC measurements with R^2 ranging from 0.39 (violaxanthin) to 0.98 (Chl a) during both surveys. Alloxanthin, Chl b, and fucoxanthin exhibiting similar patterns with Chla, showed different levels of increase after Hurricane Harvey. In contrast, NNLS-derived zeaxanthin and peridinin presented significantly low values in the area where Chla concentrations were high. Further, maps of zeaxanthin and peridinin displayed relatively higher fraction on July 06, 2017 before the hurricane compared to other diagnostic pigments. However, peridinin decreased post-hurricane on September 29, 2017 and then increased a bit on October 29-30, 2017. Ultimately, concentration of Chl a and all biomarker pigments decreased to low levels in November, 2017 when the typical environmental conditions of GB was restored.

Finally, the retrieved phytoplankton taxonomic compositions from IOP inversion algorithm were linked with FIRe-measured photosynthetic parameters (F_V/F_M and σ_{PSII}) to assess the effects of physiological stress and taxonomic contributions on phytoplankton photosynthetic performance. An inverse relationship between the F_V/F_M and σ_{PSII} were observed during both surveys. Phytoplankton community in well-mixed waters (around Smith Point) showed high F_V/F_M against low σ_{PSII}; in contrast, the area with poor nutrient conditions (adjacent to the shelf waters), showed low F_V/F_M and elevated σ_{PSII}. Taxonomic signatures of F_v/F_m and σ_{PSII} revealed diverse physiological characteristics with dinoflagellate-haptophyte group showing the lowest F_V/F_M versus the highest σ_{PSII}, whereas prokaryote of cyanobacteria-dominated group showed high values of F_V/F_M and low values of σ_{PSII}. Overall, this study using field and ocean color data combined with inversion algorithms provided novel insights on phytoplankton response to an extreme flood perturbation in a turbid estuarine environment based on taxonomy, pigment composition and physiological state of phytoplankton.

Data availability. Data from field measurements are available upon request from the corresponding author.

Author contributions. BL and ED conceived and designed the research; BL, ED and IJ collected and processed the data; BL analyzed the data and all authors contributed to writing the paper.

Competing interests. The authors declare that they have no conflict of interest.

Acknowledgements. The authors thank the European Space Agency (ESA) and the European Organization for Meteorological Satellites (EUMESAT) for providing access to the Sentinel-3 OLCI ocean color data and the Sentinel-3 Toolbox Kit Module (S3TBX) version 5.0.1 in Sentinel Application Platform (SNAP). We also would like to thank Phytoplankton Dynamics Lab of Texas A&M University, Galveston Campus, for the near-real time microplankton pictures recorded by an Imaging FlowCytobot, which are made available on the web. We are also grateful to Bill Gibson from the Coastal Studies Institute for providing logistic support for field operations. EJD acknowledges NASA support through grant No. 80NSSC18K0177.

References

Acker, J., Lyon, P., Hoge, F., Shen, S., Roffer, M., and Gawlikowski, G.: Interaction of Hurricane Katrina with optically complex water in the Gulf of Mexico: interpretation using satellite-derived inherent optical properties and chlorophyll concentration, IEEE Geosci. and Remote Sens. Lett., 6, 209-213, 2009.

Aiken, J., Fishwick, J., Moore, G., and Pemberton, K.: The annual cycle of phytoplankton photosynthetic quantum efficiency, pigment composition and optical properties in the western English Channel, J. Mar. Biol. Assoc. U. K., 84, 301-313, 2004.

Alvain, S., Moulin, C., Dandonneau, Y., and Bréon, F.-M.: Remote sensing of phytoplankton groups in case 1 waters from global SeaWiFS imagery, Deep Sea Res., Part I, 52, 1989-2004, 2005.

Barlow, R., Cummings, D., and Gibb, S.: Improved resolution of mono-and divinyl chlorophylls a and b and zeaxanthin and lutein in phytoplankton extracts using reverse phase C-8 HPLC, Mar. Ecol. Progr. Ser., 161, 303-307, 1997.

Behrenfeld, M. J., and Falkowski, P. G.: Photosynthetic rates derived from satellite-based chlorophyll concentration, Limnol. Oceanogr., 42, 1-20, 1997.

Behrenfeld, M. J., and Kolber, Z. S.: Widespread iron limitation of phytoplankton in the South Pacific Ocean, Science, 283, 840-843, 1999.

886 Berman-Frank, I., Quigg, A., Finkel, Z. V., Irwin, A. J., and Haramaty, L.: Nitrogen-fixation strategies and Fe
887 requirements in cyanobacteria, Limnol. Oceanogr., 52, 2260-2269, 2007.
888 Bidigare, R. R., Ondrusek, M. E., Morrow, J. H., and Kiefer, D. A.: In-vivo absorption properties of algal
889 pigments, Ocean Optics X, Intl. Soc. Opt. Photonics., 1302, 290-303, 1990.
890 Blondeau-Patissier, D., Gower, J. F., Dekker, A. G., Phinn, S. R., and Brando, V. E.: A review of ocean color
891 remote sensing methods and statistical techniques for the detection, mapping and analysis of phytoplankton blooms
892 in coastal and open oceans, Progr. Oceanogr., 123, 123-144, 2014.
893 Bracher, A., Taylor, M., Taylor, B., Dinter, T., Roettgers, R., and Steinmetz, F.: Using empirical orthogonal
894 functions derived from remote sensing reflectance for the prediction of phytoplankton pigments concentrations,
895 Ocean Sci., 11, 139-158, 2015.
896 Brewin, R. J., Sathyendranath, S., Hirata, T., Lavender, S. J., Barciela, R. M., and Hardman-Mountford, N. J.: A
897 three-component model of phytoplankton size class for the Atlantic Ocean, Ecol. Modell., 221, 1472-1483, 2010.
898 Bricaud, A., Claustre, H., Ras, J., and Oubelkheir, K.: Natural variability of phytoplanktonic absorption in oceanic
899 waters: Influence of the size structure of algal populations, J. Geophys. Res. Oceans, 109, C11010–1, 2004.
900 Campbell, D., Hurry, V., Clarke, A. K., Gustafsson, P., and. Öquist, G.: Chlorophyll fluorescence analysis of
901 cyanobacterial photosynthesis and acclimation, Microbiol. Molecul. Biol. Rev., 62, 667-683, 1988.
902 Carder, K. L., Chen, F., Lee, Z., Hawes, S., and Kamykowski, D.: Semianalytic Moderate-Resolution Imaging
903 Spectrometer algorithms for chlorophyll a and absorption with bio-optical domains based on nitrate-depletion
904 temperatures, J. Geophys. Res. Oceans, 104, 5403-5421, 1999.
905 Chase, A., Boss, E., Zaneveld, R., Bricaud, A., Claustre, H., Ras, J., Dall'Olmo, G., and Westberry, T. K.:
906 Decomposition of in situ particulate absorption spectra, Meth. Oceanogr., 7, 110-124, 2013.
907 Chase, A., Boss, E., Cetinić, I., and Slade, W.: Estimation of phytoplankton accessory pigments from hyperspectral
908 reflectance spectra: toward a global algorithm, J. Geophys. Res. Oceans, 122, 9725-9743, 2017.
909 Ciotti, A. M., Lewis, M. R., and Cullen, J. J.: Assessment of the relationships between dominant cell size in natural
910 phytoplankton communities and the spectral shape of the absorption coefficient, Limnol. Oceanogr., 47, 404-417,
911 2002.
912 Cullen, J. J., and Davis, R. F.: The blank can make a big difference in oceanographic measurements, Limnol.
913 Oceanogr., 12, 29-35, 2003.
914 D'Sa, E. J., Lohrenz, S. E., Asper, V. L., and Walters, R. A.: Time series measurements of chlorophyll fluorescence
915 in the oceanic bottom boundary layer with a multisensor fiber-optic fluorometer, J. Atmos. Ocean. Technol., 14,
916 889-896, 1997.
917 D'Sa, E. J., and Lohrenz, S. E.: Theoretical treatment of fluorescence detection by a dual-fiber-optic sensor with
918 consideration of sampling variability and package effects associated with particles, Appl. Optics, 38, 2524-2535,
919 1999.
920 D'Sa, E. J., Miller, R. L., and Del Castillo, C.: Bio-optical properties and ocean color algorithms for coastal waters
921 influenced by the Mississippi River during a cold front, Appl. Optics, 45, 7410-7428, 2006.
922 D'Sa, E. J., Korobkin, M., and Ko, D. S.: Effects of Hurricane Ike on the Louisiana–Texas coast from satellite and
923 model data, Remote Sens. Lett., 2, 11-19, 2011.
924 D'Sa, E. J.: Assessment of chlorophyll variability along the Louisiana coast using multi-satellite data, GISci. Remote
925 Sens., 51, 139-157, 2014.
926 D'Sa, E. J., Joshi, I., and Liu, B.: Galveston Bay and coastal ocean optical- geochemical response to Hurricane
927 Harvey from VIIRS ocean color, Geophys. Res. Lett., 45, 10579-10589, https://doi.org/10.1029/2018GL079954,
928 2018.
929 Devred, E., Sathyendranath, S., Stuart, V., and Platt, T.: A three component classification of phytoplankton
930 absorption spectra: Application to ocean-color data, Remote Sens. Environ., 115, 2255-2266, 2011.
931 Dierssen, H. M., Kudela, R. M., Ryan, J. P., and Zimmerman, R. C.: Red and black tides: Quantitative analysis of
932 water-leaving radiance and perceived color for phytoplankton, colored dissolved organic matter, and suspended
933 sediments, Limnol. Oceanogr., 51, 2646-2659, 2006.
934 Doerffer, R., and Schiller, H.: The MERIS Case 2 water algorithm, Intl. J. Remote Sens., 28, 517-535, 2007.
935 Dorado, S., Booe, T., Steichen, J., McInnes, A. S., Windham, R., Shepard, A., Lucchese, A. E., Preischel, H.,
936 Pinckney, J. L., and Davis, S. E.: Towards an understanding of the interactions between freshwater inflows and
937 phytoplankton communities in a subtropical estuary in the Gulf of Mexico, PLoS One, 10, e0130931, 2015.
938 Dugdale, R., Wilkerson, F., Parker, A. E., Marchi, A., and Taberski, K.: River flow and ammonium discharge
939 determine spring phytoplankton blooms in an urbanized estuary, Estuar. Coast. Shelf Sci., 115, 187-199, 2012.

Dutkiewicz, S., Hickman, A. E., Jahn, O., Gregg, W. W., Mouw, C. B., and Follows, M. J.: Capturing optically important constituents and properties in a marine biogeochemical and ecosystem model, Biogeosciences, 12, 4447-4481, 2015.
Farfan, L. M., D'Sa, E. J., and Liu, K.: Tropical cyclone impacts on coastal regions: the case of the Yucatan and the Baja California Peninsulas. Mexico, Estuar. Coast., 37, 1388-1402, 2014.
Ficek, D., Kaczmarek, S. a., Stoñ-Egiert, J., Wozniak, B., Majchrowski, R., and Dera, J.: Spectra of light absorption by phytoplankton pigments in the Baltic; conclusions to be drawn from a Gaussian analysis of empirical data, Oceanologia, 46, 533-555, 2004.
Fishwick, J. R., Aiken, J., Barlow, R., Sessions, H., Bernard, S., and Ras, J.: Functional relationships and bio-optical properties derived from phytoplankton pigments, optical and photosynthetic parameters; a case study of the Benguela ecosystem, J. Mar. Biol. Assoc. U. K., 86, 1267-1280, 2006.
Garver, S. A., and Siegel, D. A.: Inherent optical property inversion of ocean color spectra and its biogeochemical interpretation: 1. Time series from the Sargasso Sea, J. Geophys. Res., Oceans, 102, 18607-18625, 1997.
Geider, R. J., La Roche, J., Greene, R. M., and Olaizola, M.: Response of the photosynthetic apparatus of phaeodactylum tricornutum (bacillariophyceae to nitrate, phosphate, or iron starvation, J. Phycol., 29, 755-766, 1993.
Gilerson, A. A., Gitelson, A. A., Zhou, J., Gurlin, D., Moses, W., Ioannou, I., and Ahmed, S. A.: Algorithms for remote estimation of chlorophyll-a in coastal and inland waters using red and near infrared bands, Opt. Express, 18, 24109-24125, 2010.
Gitelson, A.: The peak near 700 nm on radiance spectra of algae and water: relationships of its magnitude and position with chlorophyll concentration, Int. J. Remote Sens., 13, 3367-3373, 1992.
Gordon, H. R., Brown, O. B., Evans, R. H., Brown, J. W., Smith, R. C., Baker, K. S., and Clark, D. K.: A semianalytic radiance model of ocean color, J. Geophys. Res., Atmos., 93, 10909-10924, 1988.
Guthrie, C. G., Matsumoto, J., and Solis, R.: Analysis of the influence of water plan strategies on inflows and salinity in Galveston Bay, Final report to the United States Army Corps of Engineers, Contract #R0100010015. Texas Water Development Board, Austin, Texas, USA, 71 pp., 2012.
Heisler, J., Glibert, P. M., Burkholder, J. M., Anderson, D. M., Cochlan, W., Dennison, W. C., and Lewitus, A.: Eutrophication and harmful algal blooms: a scientific consensus, Harmful Algae, 8, 3-13, 2008.
Hirata, T., Aiken, J., Hardman-Mountford, N., Smyth, T. J., and. Barlow, R. G.: An absorption model to determine phytoplankton size classes from satellite ocean colour, Remote Sens. Environ., 112, 3153–3159, 2008.
Hirata, T., Hardman-Mountford, N., Brewin, R., Aiken, J., Barlow, R., Suzuki, K., Isada, T., Howell, E., Hashioka, T., Noguchi-Aita, M., and Yamanaka, Y.: Synoptic relationships between surface Chlorophyll-a and diagnostic pigments specific to phytoplankton functional types. Biogeosciences, 8, 311–327, 2011.
Hoepffner, N., and Sathyendranath, S.: Effect of pigment composition on absorption properties of phytoplankton, Mar. Ecol. Progr. Ser., 73, l-23, 1991.
Hoge, F. E., and Lyon, P. E.: Satellite retrieval of inherent optical properties by linear matrix inversion of oceanic radiance models: an analysis of model and radiance measurement errors, J. Geophys. Res., Oceans, 101, 16631-16648, 1996.
Holmboe, N., Jensen, H. S., and Andersen, F. Ø.: Nutrient addition bioassays as indicators of nutrient limitation of phytoplankton in a eutrophic estuary, Mar. Ecol. Progr. Ser., 186, 95-104, 1999.
Howarth, R. W., Marino, R., Lane, J., and Cole, J. J.: Nitrogen fixation in freshwater, estuarine, and marine ecosystems. 1. Rates and importance, Limnol. Oceanogr., 33, 669-687, 1988.
Hu, C., Cannizzaro, J., Carder, K. L., Muller-Karger, F. E., and Hardy, R.: Remote detection of Trichodesmium blooms in optically complex coastal waters: Examples with MODIS full-spectral data, Remote Sens. Environ., 114, 2048-2058, 2010.
Hu, C., and Feng, L.: Modified MODIS fluorescence line height data product to improve image interpretation for red tide monitoring in the eastern Gulf of Mexico, J. Appl. Remote Sens., 11, 012003, 2016.
Jeffrey, S., and Vest, M.: Introduction to marine phytoplankton and their pigment signatures, in: Phytoplankton pigment in oceanography, edited by: Jeffrey, S.W., Mantoura, R. F. C., and Wright, S. W., UNESCO Publishing, Paris, France, 37-84, 1997.
Joshi, I. D., and D'Sa, E. J.: Seasonal variation of colored dissolved organic matter in Barataria Bay, Louisiana, using combined Landsat and field data, Remote Sens., 7, 12478-12502, 2015.
Joshi, I. D., D'Sa, E. J., Osburn, C. L., Bianchi, T. S., Ko, D. S., Oviedo-Vargas, D., Arellano, A. R., and Ward, N. D.: Assessing chromophoric dissolved organic matter (CDOM) distribution, stocks, and fluxes in Apalachicola Bay using combined field, VIIRS ocean color, and model observations, Remote Sens. Environ., 191, 359-372, 2017.

Joshi, I. D., and D'Sa, E. J.: An estuarine tuned Quasi-Analytical Algorithm for VIIRS (QAA-V): assessment and application to satellite estimates of SPM in Galveston Bay following Hurricane Harvey. Biogeosciences, 15, 4065-4086, 2018.
Kolber, Z. S., Zehr, J., and Falkowski, P. G.: Effects of growth irradiance and nitrogen limitation on photosynthetic energy conversion in photosystem II, Plant Physiol., 88, 923-929, 1988.
Kolber, Z. S., Prášil, O., and Falkowski, P. G.: Measurements of variable chlorophyll fluorescence using fast repetition rate techniques: defining methodology and experimental protocols, Biochim. Biophys. Acta (BBA)-Bioenergetics, 1367, 88-106, 1998.
Latasa, M., and Bidigare, R. R.: A comparison of phytoplankton populations of the Arabian Sea during the Spring Intermonsoon and Southwest Monsoon of 1995 as described by HPLC-analyzed pigments, Deep Sea Res., Part II, 45, 2133-2170, 1998.
Lee, Z., Carder, K. L., Peacock, T., Davis, C., and Mueller, J.: Method to derive ocean absorption coefficients from remote-sensing reflectance, Appl. Optics, 35, 453-462, 1996.
Lee, Z., Carder, K. L., and Arnone, R. A.: Deriving inherent optical properties from water color: a multiband quasi-analytical algorithm for optically deep waters, Appl. Optics, 41, 5755-5772, 2002.
Lee, H. A.: Effects of Physical Disturbance on Phytoplankton Diversity and Community Composition in Galveston Bay, TX, during an Extreme Flooding Event, Diss., 2017.
Lohrenz, S. E., Weidemann, A. D., and Tuel, M.: Phytoplankton spectral absorption as influenced by community size structure and pigment composition J. Plankton Res., 25, 35-61, 2003.
Lutz, V. A., Sathyendaranath, S., Head, E. J., and Li, W. K.: Changes in the in vivo absorption and fluorescence excitation spectra with growth irradiance in three species of phytoplankton, J. Plankton Res., 23, 555-569, 2001.
Mackey, M., Mackey, D., Higgins, H., and Wright, S.: CHEMTAX-a program for estimating class abundances from chemical markers: application to HPLC measurements of phytoplankton, Mar. Ecol. Progr. Ser., 144, 265-283, 1996.
Maritorena, S., Siegel, D. A., and Peterson, A. R.: Optimization of a semianalytical ocean color model for global-scale applications, Appl. Optics, 41, 2705-2714, 2002.
Moisan, T. A., Moisan, J. R., Linkswiler, M. A., and Steinhardt, R. A.: Algorithm development for predicting biodiversity based on phytoplankton absorption, Cont. Shelf Res., 55, 17-28, 2013.
Moisan, T. A., Rufty, K. M., Moisan, J. R., and Linkswiler, M. A.: Satellite observations of phytoplankton functional type spatial distributions, phenology, diversity, and ecotones, Front. Mar. Sci., 4, 189, 2017.
Moore, C. M., Suggett, D. J., Holligan, P. M., Sharples, J., Abraham, E. R., Lucas, M. I., Rippeth, T. P., Fisher, N. R., Simpson, J. H., and Hydes, D. J.: Physical controls on phytoplankton physiology and production at a shelf sea front: a fast repetition-rate fluorometer based field study, Mar. Ecol. Progr. Ser., 259, 29-45, 2003.
Moore, C. M., Suggett, D. J., Hickman, A. E., Kim, Y.-N., Tweddle, J. F., Sharples, J., Geider, R. J., and Holligan, P. M.: Phytoplankton photoacclimation and photoadaptation in response to environmental gradients in a shelf sea, Limnology and Oceanography, 51, 936-949, 2006.
Morel, A., and Prieur, L.: Analysis of variations in ocean color 1, Limnol. Oceanogr., 22, 709-722, 1977.
Nair, A., Sathyendranath, S., Platt, T., Morales, J., Stuart, V., Forget, M.-H., Devred, E., and Bouman, H.: Remote sensing of phytoplankton functional types, Remote Sens. Environ., 112, 3366-3375, 2008.
Örnólfsdóttir, E. B., Pinckney, J. L., and Tester, P. A.: Quantification of the relative abundance of the toxic dinoflagellate, karenia brevis (dinophyta), using unique photopigments, J. Phycol., 39, 449-457, 2003.
Örnólfsdóttir, E. B., Lumsden, S. E., and Pinckney, J. L.: Nutrient pulsing as a regulator of phytoplankton abundance and community composition in Galveston Bay, Texas, J. Experiment. Mar. Biol. Ecol., 303, 197-220, 2004a.
Örnólfsdóttir, E. B., Lumsden, S. E., and Pinckney, J. L.: Phytoplankton community growth-rate response to nutrient pulses in a shallow turbid estuary, Galveston Bay, Texas, J. Plankton Res., 26, 325-339, 2004b.
Paerl, H. W., Valdes, L. M., Pinckney, J. L., Piehler, M. F., Dyble, J., and Moisander, P. H.: Phytoplankton photopigments as indicators of estuarine and coastal eutrophication, AIBS Bull., 53, 953-964, 2003.
Pan, X., Mannino, A., Russ, M. E., Hooker, S. B., and Harding Jr, L. W.: Remote sensing of phytoplankton pigment distribution in the United States northeast coast, Remote Sens. Environ., 114, 2403-2416, 2010.
Pan, X., Mannino, A., Marshall, H. G., Filippino, K. C., and Mulholland, M. R.: Remote sensing of phytoplankton community composition along the northeast coast of the United States, Remote Sens. Environ., 115, 3731-3747, 2011.
Quigg, A., Roelke, D., and Davis, S. E.: Freshwater inflows and the health of Galveston Bay: influence of nutrient and sediment load on the base of the food web, Final report of the coastal coordination council pursuant to National Oceanic and Atmospheric Administration Award No. NA07NOS4190144, Texas A&M University at Galveston, Texas, USA, 49 pp., 2009.

Quigg, A., Litherland, S., Phillips, J., and Kevekordes, K.: Phytoplankton productivity across Moreton Bay, Queensland, Australia: the impact of water quality, light and nutrients on spatial patterns, in: Proceedings of the 13th International Marine Biological Workshop, Moreton Bay, Queensland, Australia, 7-25 February, 2005, 355-372, 2010.

Quigg, A. S.: Understanding the role of nutrients in defining phytoplankton responses in the Trinity-San Jacinto Estuary, Final report to Interagency Cooperative Contract No. 1104831134, Texas A & M University at Galveston, Texas, USA, 56 pp., 2011.

Rayson, M. D., Gross, E. S., Hetland, R. D., and Fringer, O. B.: Time scales in Galveston Bay: An unsteady estuary, J. Geophys. Res., Oceans, 121, 2268–2285, 2016.

Ritchie, R. J.: Consistent sets of spectrophotometric chlorophyll equations for acetone, methanol and ethanol solvents, Photosynthesis Res., 89, 27-41, 2006.

Roelke, D. L., Li, H.-P., Hayden, N. J., Miller, C. J., Davis, S. E., Quigg, A., and Buyukates, Y.: Co-occurring and opposing freshwater inflow effects on phytoplankton biomass, productivity and community composition of Galveston Bay, USA, Mar. Ecol. Progr. Ser., 477, 61-76, 2013.

Roesler, C. S., and Perry, M. J.: In situ phytoplankton absorption, fluorescence emission, and particulate backscattering spectra determined from reflectance, J. Geophys. Res., Oceans, 100, 13279-13294, 1995.

Roesler, C. S., and Boss, E.: Spectral beam attenuation coefficient retrieved from ocean color inversion, Geophys. Res. Lett., 30, 2003.

Roesler, C. S., Etheridge, S. M., and Pitcher, G. C.: Application of an ocean color algal taxa detection model to red tides in the Southern Benguela, in: Proceedings of the Xth International Conference on Harmful Algae, Florida Fish and Wildlife Conservation Commission and Intergovernmental Oceanographic Commission of UNESCO, St. Petersburg, Florida, USA, October, 2002, 303-305, 2003.

Roy, E. D., White, J. R., Smith, E. A., Bargu, S., and Li, C.: Estuarine ecosystem response to three large-scale Mississippi River flood diversion events, Sci. Total Environ., 458, 374-387, 2013.

Santschi, P. H.: Seasonality in nutrient concentrations in Galveston Bay, Mar. Environ. Res., 40, 337-362, 1995.

Sathyendranath, S., Aiken, J., Alvain, S., Barlow, R., Bouman, H., Bracher, A., Brewin, R., Bricaud, A., Brown, C., and Ciotti, A.: Phytoplankton functional types from Space, in: (Reports of the International Ocean-Colour Coordinating Group (IOCCG); 15), International Ocean-Colour Coordinating Group, 1-156, 2014.

Schindler, D. W.: Evolution of phosphorus limitation in lakes, Science, 196, 260–262, 1977.

Schitüter, L., Riemann, B., and Søndergaard, M.: Nutrient limitation in relation to phytoplankton carotenoid/chiorophyll a ratios in freshwater mesocosms, J. Plankton Res., 19, 891-906, 1997.

Smayda, T. J.: Harmful algal blooms: their ecophysiology and general relevance to phytoplankton blooms in the sea, Limnol. Oceanogr., 42, 1137–1153, 1997.

Steichen, J. L., Denby, A., Windham, R., Brinkmeyer, R., and Quigg, A.: A tale of two ports: Dinoflagellate and diatom communities found in the high ship traffic region of Galveston Bay, Texas (USA), J. Coastal Res., 31(2), 407-416, 2015.

Steichen, J. L., Windham, R., Hala, D., Kaiser, K., Labonte, J. M., Petersen, L. H., Bacosa, H., Bretherton, L., Kamalanathan, M., Setta, S., and Quigg, A.: Rapid physicochemical and biological assessment of Galveston Bay in the wake of Hurricane Harvey, abstract#AI44D-3023, in: Ocean Sciences Meeting 2018, American Geophysical Union, Portland, Oregon, USA, February, 2018.

Stramski, D., Reynolds, R. A., Kaczmarek, S., Uitz, J., and Zheng, G.: Correction of pathlength amplification in the filter-pad technique for measurements of particulate absorption coefficient in the visible spectral region, Appl. Optics, 54, 6763-6782, 2015.

Suggett, D. J., Warner, M. E., Smith, D. J., Davey, P., Hennige, S., and Baker, N. R.: Photosynthesis and production of hydrogen peroxide by Symbiodinium (pyrrhophyta) phylotypes with different thermal tolerances 1, J. Phycol, 44, 948-956, 2008.

Suggett, D. J., Moore, C. M., Hickman, A. E., and Geider, R. J.: Interpretation of fast repetition rate (FRR) fluorescence: signatures of phytoplankton community structure versus physiological state, Mar. Ecol. Progr. Ser., 376, 1-19, 2009.

Sun, D., Huan, Y., Qiu, Z., Hu, C., Wang, S., and He, Y.: Remote-sensing estimation of phytoplankton size classes from GOCI satellite measurements in Bohai Sea and Yellow Sea, J. Geophys. Res. Oceans, 122, 8309-8325, 2017.

Thrane, J.-E., Kyle, M., Striebel, M., Haande, S., Grung, M., Rohrlack, T., and Andersen, T.: Spectrophotometric analysis of pigments: a critical assessment of a high-throughput method for analysis of algal pigment mixtures by spectral deconvolution, PloS one, 10, e0137645, 2015.

Wang, G., Lee, Z., Mishra, D. R., and Ma, R.: Retrieving absorption coefficients of multiple phytoplankton pigments from hyperspectral remote sensing reflectance measured over cyanobacteria bloom waters, Limnol. Oceanogr., Meth., 14, 432-447, 2016.
Wright, S. W., and Jeffrey, S. W.: Pigment markers for phytoplankton production, in: Marine organic matter: biomarkers, isotopes and DNA, The Handbook of Environmental Chemistry, edited by Volkman, J. K., Springer, Berlin, Heidelberg, Germany, 71-104, 2006.